UNIVERSITY OF OKLAHOMA
GRADUATE COLLEGE

MODELLING OSCILLATORY FLOW IN A CONE-AND-PLATE DEVICE USING COMPUTATIONAL FLUID DYNAMICS

A THESIS
SUBMITTED TO THE GRADUATE FACULTY
in partial fulfillment of the requirements for the
Degree of
MASTER OF SCIENCE

By

EMAD RAMADAN
Norman, Oklahoma
2019

MODELLING OSCILLATORY FLOW IN A CONE-AND-PLATE DEVICE USING COMPUTATIONAL FLUID DYNAMICS

A THESIS APPROVED FOR THE
SCHOOL OF CHEMICAL, BIOLOGICAL AND MATERIALS ENGINEERING

BY

Dr. Matthias U. Nollert, Chair

Dr. Dimitrios V. Papavassiliou

Dr. Dibbon K. Walters

Acknowledgements

I dedicate this work to my parents Seif and Amal. I would not have done this without their love, support, and trust. For that I would like to take this opportunity to extend my deepest gratitude to them.

I would like to particularly thank my advisor Dr. Nollert for taking me on as a Master's student. Dr. Nollert has been extraordinarily tolerant and supportive, and for that I am very grateful. I extend my gratitude to my committee members Dr. Walters and Dr. Papavassiliou as their advice and comments has been of immense help in my journey of learning Fluent.

Table of Contents

List Of Figures

List Of Tables

Abstract

Calcific aortic heart valve disease has been investigated in literature over the past three decades. Researches have been trying to understand the mechanism by which the calcification occurs on the aortic valve leaflets. Mechanical forces due to the flow of blood have been shown to have a significant contribution to the calcification of the leaflets, however, no one was able to study the native mechanical environment in the heart valve due to the complexity of the geometry. There is a soluble factor that is a known precursor for the disease called Transforming Growth Factor-β1. TGF-β1 is a protein which exists in large amounts in platelets that are flowing in the blood. The mechanism by which TGF-β1 activates and contributes to the disease is not known, but its known that calcification is seen in areas were disturbed flow exists. This disturbed flow is defined as low and oscillatory shear environment, therefore, researches studied the activation of TGF-β1 under oscillatory shear versus steady shear using a cone and plate device. There is, however, a lot of ambiguity in the way one produces oscillatory shear in a cone and plate. In this thesis we first study a simple geometry of a parallel plate. We see that abruptly stopping the plate to change directions of translation yields two spikes in the volume averaged shear rate that are 1.6 and 1.2 times higher than the average when stopping and restarting the movement of the plate, respectively. Areas of the fluid which experience elevated shear rates compared to the average constitute 65 percent of the volume of the fluid in the parallel plate. A different shear rate profile was seen when the plate was linearly decelerated to zero then re-accelerated to translate in the opposite direction. We only saw one peak which was 1.3 times higher than the average value with 20 percent by volume of the fluid experiencing shear rate value higher than the average value of 380 s^{-1}. Moreover, a sinusoidal oscillation of the plate did not show any spike in the shear rate and

98 percent of the fluid, at the end of the stopping period, experienced shear rate values between 107 s^{-1} and 120 s^{-1} where the minimum and maximum shear rate values were 106.2 s^{-1} and 120.2 s^{-1} . We then studied the more complicated geometry of the cone and plate and saw similar behaviors in the volume averaged shear rate profiles compared to those computed in the parallel plate case. Abruptly stopping the cone showed two spikes upon stopping and starting that were both 1.6 times higher than the average. At the end of the sinusoidal rotation we computed a volume averaged value of 175 s^{-1} with a minimum shear rate value of 0.001 s^{-1} and 963 s^{-1}. We further computed that 5 percent of the fluid is experiencing shear rate values that are 2x the average value or higher. In the case of the linear deceleration/acceleration, we saw a peak that is 1.7 times higher than the average. We computed that at the end of the stopping period the volume averaged shear rate value is 380 s^{-1} with a minimum shear rate value of 0.6 s^{-1} and a maximum value of 3973 s^{-1}. We further computed that 13 percent of the fluid experiences values of shear rate that are 2x the average value or higher. In the case of the sinusoidal rotation, no spikes in shear rate were seen. At the end of the sinusoidal oscillation, we computed a minimum shear rate value of 0.6 s^{-1}, a maximum shear rate value of 1690 s^{-1}, and a volume averaged shear rate value of 350 s^{-1}. We further computed that 5 percent of the fluid experiences shear rate values that are 2x the average or higher.

Chapter 1

Introduction

1.1 Introduction

As the number of elderly patients with calcific aortic valve disease (CAVD) is expected to double by 2050, CAVD remains the reason behind 30 000 deaths and 77 000 hospital discharges, annually.(Benjamin et al. 2018) CAVD is defined as a pathological change in the aortic valve biology which is the cause of backflow of blood into the left ventricle or lower blood flow from the left ventricle to the vascular system. The calcification of the valve is characterized as the formation of calcific lesions on the surface of the valve leaflets which render the valve leaflets stiff and thus obstructing the outflow of blood from the left ventricle leading to heart failure.(Sun et al. 2013) Currently, the only way to treat CAVD is through an invasive surgery procedure where the calcified valve is replaced with a prosthetic one. The mechanism by which CAVD occurs is poorly understood and much research in the past 20 years has been done to investigate the biological pathways by which the calcific lesions form on the leaflets. The calcification of the aortic valve is said to be side-specific; where the aortic side of the valve is preferentially calcified leaving the ventricular side uncalcified (Fernández Esmerats et al. 2016). The side specificity is explained in terms of the direction and magnitude of the force applied due to the velocity gradient in the flow of blood passing along the endothelium wall from the left ventricle

to the aorta; this force is known as the shear stress. The current hypothesis is that the ventricular side is exposed to steady flow which is characterized as unidirectional high magnitude and pulsatile shear stress while the fibrosa side is exposed to disturbed flow (d-flow) which is characterized by low magnitude and oscillatory shear stress (Esmerats et al. 2019). On one hand, the unidirectional, high magnitude, and pulsatile shear stress was found to be beneficial for the endothelium wall as it contributes to valvular homeostasis by regulating valvular biosynthetic activity and endothelial cell alignment(Sun et al. 2013). On the other hand, bi-directional and oscillatory shear stress is known to increase inflammation and endothelial dysfunction leading to the formation of calcific lesions (Fernández Esmerats et al. 2016). Therefore, shear stress is known to play a crucial role in endothelial cell function. Many mechanosensitive genes have been found when testing the response of endothelial cells to applied shear stress. Transforming growth factor-B1 ligand and receptors are known as key factors in aortic calcification and inducing endothelial cell inflammatory phenotype. Many studies have shown that the levels of TGF-β1 in the blood of patients with CAVD are nearly three folds higher than in healthy patients. Therefore, many researchers studied the effect of shear stress on TGF-β1 to try to understand the mechanism by which this molecule contributes to the calcification. Most of the TGF-β1 does not come from endothelial cells, however. Platelets are known to have a concentration of TGF-β1 that is (40-100)x more than any other cells. As platelets flow with the blood and are the main source of TGF-β1, we are interested in the volume averaged shear stress and its effect on TGF-β1. When TGF-β1 is subjected to shear stress the release of latent (inactive) TGF-β1 increases and TGF-β1 switches from its latent to active form through an unknown pathway. The activated TGF-β1 plays a fundamental role in leading

to fibrosis and calcification (Wang et al. 2014) The levels of activated TGF-β1 are much higher when TGF-β1 is subjected to disturbed flow compared to steady flow (Kouzbari et al. 2019). In order to understand the mechanism by which TGF-β1 activates, one must investigate the response of TGF-β1 when its exposed to steady flow as well as disturbed flow. The device with which researchers use to apply a uniform shear stress is known as a Cone-and-Plate device (CPD). CPDs have been widely used in biomedical research for the past three to four decades and were first developed by Dewey et al. (1981) to test endothelial cells in the lab. A CPD consists of an inverted cone that has its apex held a distance h above the cone and the cells to be tested are either in suspension or adhered to the surface of the plate. The cone is then rotated with a chosen RPM (rotations per minute) in order to apply a uniform shear stress across the entire fluid in the devices chamber. In order to produce a unidirectional shear stress, the cone is rotated in either clockwise or counter-clockwise direction. The unidirectional steady rotation of the cone is well-characterized in literature and well-defined analytical solutions exist (Sdougos et al. 1984),(Sucosky et al. 2008). For the bidirectional rotation of the cone, analytical solutions are poorly defined in literature due to the complexity of transient state problems. Moreover, steady flow, as referred to in literature, is clearly defined as a steady rotation of the cone in a CPD. However, disturbed flow is not defined, and it is usually assumed as a sinusoidal function. The choice of sinusoidal rotation of the cone is often convenient because an analytical solution exists for this case, but other choices are available. The goal of this thesis is to investigate the importance of the choice and details of the time-dependent rotation of the cone on the volume averaged shear stress in the fluid.

1.1.1 The Aortic Valve

The aortic valve is the door connecting the left ventricle to the ascending aorta and consists of three semi-lunar leaflets. The Aortic valve structure consists of Endothelial cells, Interstitial cells, collagen fibers, Glycosaminoglycans (GAGs), and Elastin fibers (Figure 1.1). The fibrosa which is facing the aorta, mainly

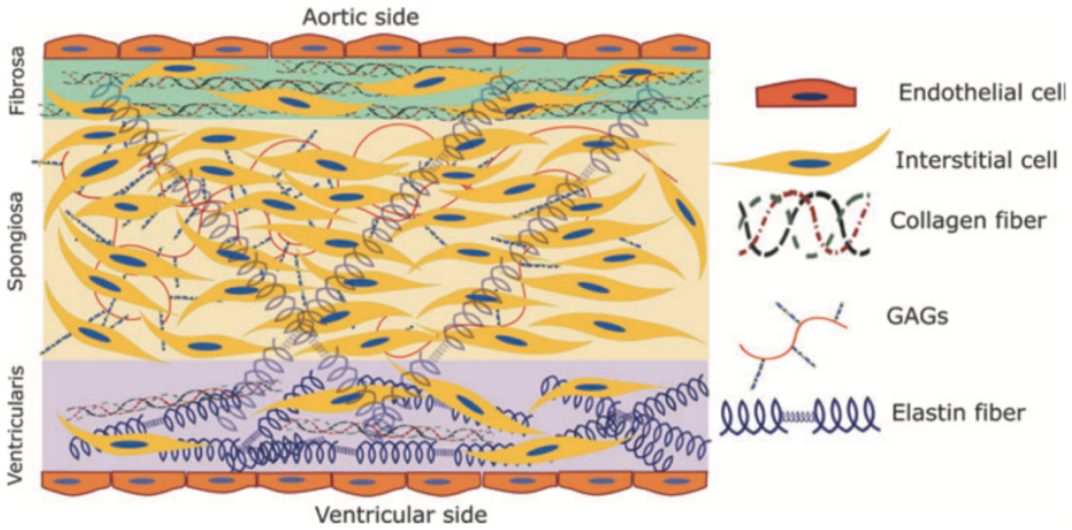

Figure 1.1: Aortic valve Structure, (Fernández Esmerats et al. 2016)

contains collagen which allows the fibrosa to bear high mechanical stresses exerted upon it during systole. The ventricular side mainly contains elastin fibers and is facing the left ventricle. The Spongiosa contains more Interstitial cells and GAGs compared to the fibrosa and ventricular side. During ventricular systole (heart muscle contraction), the aortic valve opens and allows the Oxygen-rich blood to flow into the aortic valve. However, during ventricular diastole (heart muscle relaxation), the aortic valve closes to prevent backflow of blood into the left ventricle from the aorta. (McKinley et al. 2017) The aortic valve opens and closes over 100,000 times a day, and for many years, the aortic valve was thought of as a passive structure that opens and closes due to transvalvular

pressure and ventricular contraction or relaxation. However, it is now agreed upon that the aortic valves functions follow complex mechanisms most of which are unknown or poorly understood(Chester et al. 2014) The aortic valve experiences a wide range of hydrodynamic forces. Fernández Esmerats et al. (2016), explained that the constant movement of the valve affects the valvular endothelium where the endothelial cells experience three types of forces: pressure, axial and bending stress, and shear stress. The differential pressure across the valve is significant in shaping the tissue and geometry of the valve. High blood pressure is correlated with calcification but the mechanism by which that happens remains unknown. Axial stress is critical for the prevention of blood flowing backwards into the ventricle from the ascending aorta during diastole. Shear stress regulates endothelial cell function were the cells sense the change in the extracellular surrounding environment (through changes in shear stress) and respond accordingly, (Fernández Esmerats et al. 2016).

1.1.2 The Aortic Valve Disease

The number of patients with CAVD is expected to double by 2040. According to the 2018 American Heart Association Cardiovascular statistics, factors such as smoking, old age, high blood pressure, and kidney failure are some of the main reasons behind the calcification of the aortic valve (Benjamin et al. 2018). CAVD is characterized by the stiffening, thickening and narrowing of the aortic valve as well as fibrosis and the formation of calcific lesions on the valves leaflets (shown in Figure 1.2).

Risks such as congestive heart failure and sudden cardiac death are possible at advanced stages of the disease. Until now, there is no pharmacological cure

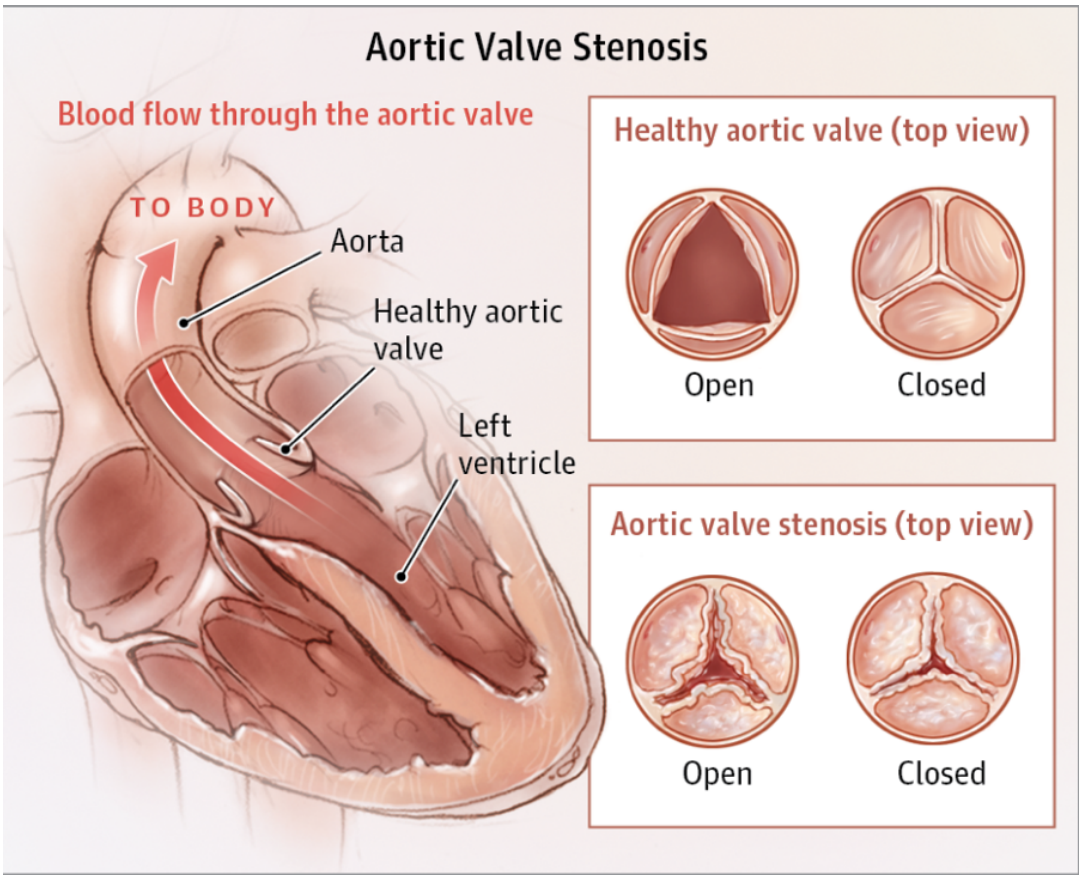

Figure 1.2: Aortic valve Disease, (Patel and Kirtane 2016)

for CAVD and no effective therapies apart from valve replacement. Valve replacement is a rather invasive surgery and less-invasive alternatives are highly desired.

1.1.3 Transforming Growth Factor TGF-β1

The family of TGF-β1 plays a critical role in many cellular responses such as growth, development, and immune system regulation (Fernández Esmerats et al. 2016) TGF-β1 is found in high concentrations in platelets. Platelets are irregular, membrane-enclosed cellular fragments that are about 2 micrometers

in diameter and are continually produced in the red bone marrow. The concentration of platelets in adults is about 150-400 thousand per microliter and they play an important role in wound healing (McKinley, 5 ed.) The plasma concentration of TGF-β1, the most abundant isoform of the TGF-β1 family, is three folds higher in patients with CAVD compared to healthy patients. Literature suggests that platelets are activated when they undergo shear stress and the shear stress due to the velocity of the blood activates the platelets inducing the release of TGF-β1 from platelets and activating the released latent (inactive) TGF-β1 (Wang et al. 2014). The rate of activation of TGF-β1 is dependent upon the nature of the shear stress applied to the platelets. A higher rate of activation of TGF-β1 was recorder when platelets undergo oscillatory shear stress compared to steady shear stress (Kouzbari et al. 2019). The mechanism by which TGF-β1 induces fibrosis and calcification is still poorly known. However, there are some known and predicted mechanisms that aid in getting a glance at the biological pathways of TGF-β1 contributing to the calcification process. Fernández Esmerats et al. (2016), explains that on the fibrosa side, where disturbed flow of blood occurs, shear activated TGF-β1 ligands and other mechanosensitive genes such as bone morphogenic proteins (BMPs) bind to their cell surface receptors on the fibrosa layer activating Smad signaling cascade by phosphorylating Smad molecules, which in turn make their way to the nucleus. Moreover, Wnt molecules and Interleukins bind to their respective cell surface receptors. Wnt molecules bind to frizzled Wnt receptors and cause the release of β-catenin which in turn translocate to the nucleus, and interleukins bind to interleukin receptors and regulate NF-kβ signaling cascade that alters gene transcription. All these pathways induce inflammation and osteogenic gene transcription while also leading to endothelial dysfunction. Anti-inflammatory

genes are not translated due to the upregulation of inflammatory miRNA in disturbed flow. Figure 1.3 is a graphical illustration of the pathways explained herein:

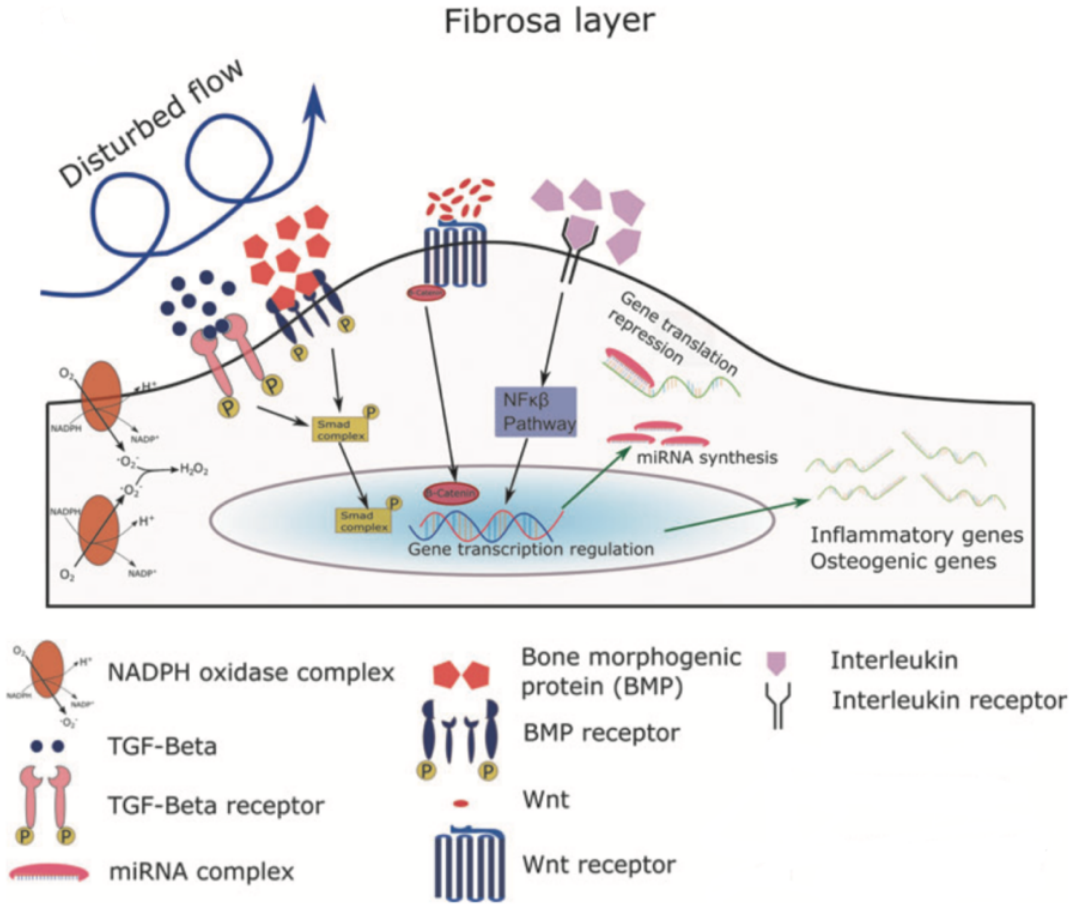

Figure 1.3: Known and predicted TGF-β1 mechanism under disturbed flow conditions, Adapted from(Fernández Esmerats et al. 2016)

Chapter 2

Fluid Mechanics

2.1 Computational Fluid Dynamics

Computational fluid dynamics is a fundamental branch of scientific research. CFD provides solutions to problems that are very difficult and often times impossible to do analytically. CFD has progressed and became a powerful tool throughout the second half of last century. It was not only until late 80s that the scientific community started to appreciate the power and effectiveness of CFD. There are many available commercial packages and the one used in this thesis is ANSYS-FLUENT. Fluent is a software used to model flow, turbulence, heat transfer, and reactions for academic and industrial applications. The Fluent solver is based on the finite volume method for solving differential equations. The domain or the geometry to be solved is discretized into a finite set of control volumes, and the general conservation equations of mass, momentum, and heat transport are solved on each of these control volumes. The partial differential equations of the Naver-Stokes equations are discretized into a system of algebraic equations which are then solved numerically to obtain the solution. There are four critical steps in the process of modelling a system: building the geometry, meshing the geometry, setting up the solver, and post-processing.

In the following two sections we show two different geometries used to study the volume averaged shear rate as a function of time. One might argue as to

why we are not solving for the flow around the heart valve geometry. The short answer is that it is complicated. The geometry of the heart valve changes with time, and medical imaging techniques such as MRI and cardiac ultrasound do not offer sufficient temporal and spatial resolution to evaluate the native fluid mechanical environment of the Aortic Valve. Moreover when modelling the aortic valve, difficulties arise in meshing fluid-solid boundary, modelling the coupled fluid-solid interaction, modelling transitional flow and turbulence, and achieving reynolds' numbers at peak flow at physiological level (Yap et al. 2012). Therefore, we use the parallel plate and cone and plate geometries to understand the time dependence of shear rate.

Referring back to our discussion in the introduction about TGF-β1 and its sensitivity to the surrounding mechanical environment; As the protein exists in platelets that are flowing with the blood through the valve we are interested in the volume averaged shear rate of the flowing fluid. Hence, when studying the parallel plate and cone and plate devices we compare how different modes of plate translation or cone rotation yield different volume averaged shear rate profiles and different regions of high shear rates. We investigate three modes of oscillating translation of the plate. First, the plate can oscillate following a sinusoidal function. Second, the plate can translate in one direction, abruptly stop for a short period of time, then translate back in the opposite direction. Last, instead of abruptly stopping the plate, the plate can linearly decelerate to zero then accelerate back to translate in the opposite direction.

Our objective is now to study how each of these modes of translation affects the volume averaged shear rate profile in the parallel plate device and whether regions of high shear stress exist or not. After that, we use the same modes of translating the plate to rotate the cone in the cone and plate device.

2.2 Parallel Plate

The parallel plate geometry is largely used in experimental work to apply fluid shear stress on living cells. Parallel plates have been widely investigated in literature and good analytical solutions exist for both the steady and unsteady case (Bird et al. 2007). The largest advantage of using a cone and plate over a parallel plate is that in a CPD the upon rotation a uniform shear stress profile is generated across the sample while the parallel plate produces a maximum shear rate at the edges and zero shear rate in the center. The parallel plate geometry is investigated in this thesis to make sure our results from the cone and plate device are consistent since the parallel plate geometry is easier to understand.

2.2.1 Building the Geometry

First a 2D sketch of the parallel plate geometry was constructed in the geometry Design-Modeler. After constructing the sketch, a 3D model was constructed by extruding the 2D sketch in the Z-direction. And thus, the following two figures are produced:

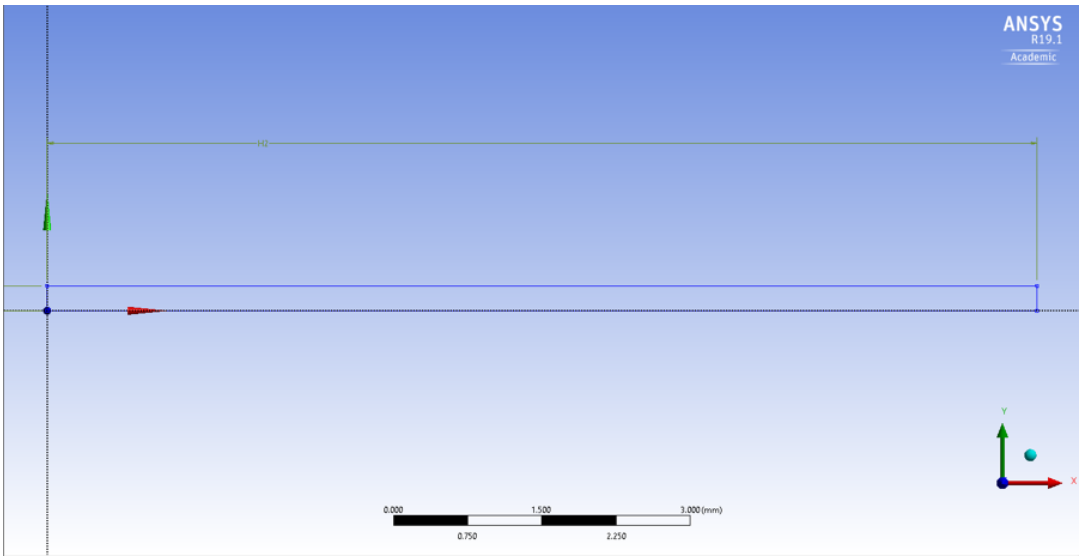

Figure 2.1: 2D sketch of Parallel Plate Geometry

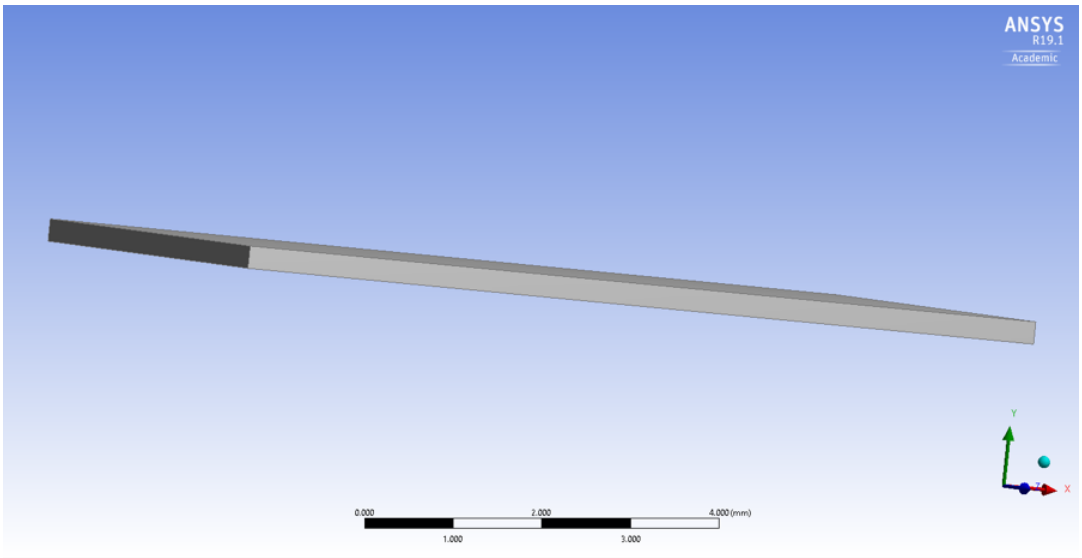

Figure 2.2: 3D model of Parallel Plate

2.2.2 Constructing the Mesh

Fluent Mesh-Modeler was used to construct the mesh. Figure 2.3 shows the generated mesh. The following mesh parameters were calculated in the meshing modeler:

- Aspect ratio: Min: 1.016, Max: 12.312, Average: 4.0284.
- Orthogonal quality: average: Min: 1.000, Max: 1.000, Average: 1.000.

For more information about the definition of these parameters, the reader is referred to Appendix C.

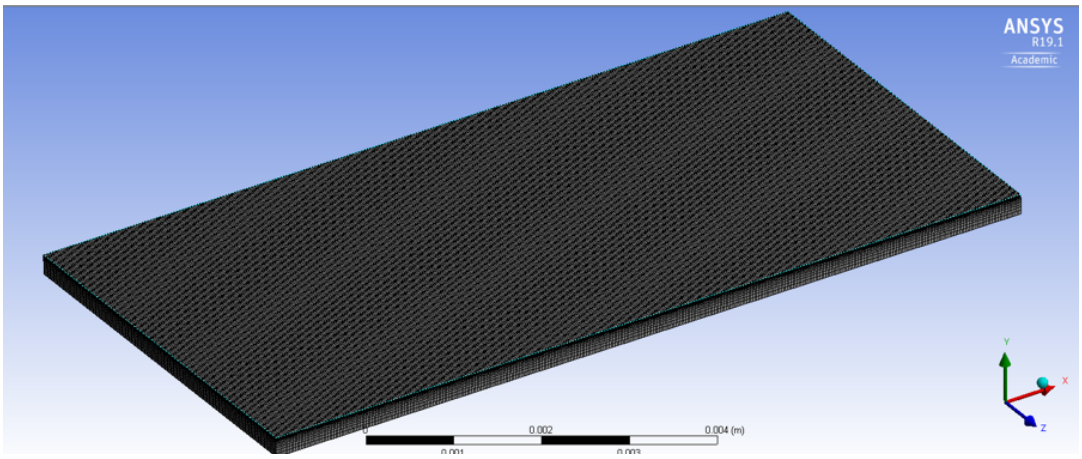

Figure 2.3: Mesh Geometry of parallel plate

2.2.3 Setting Up the Solver

After loading the mesh into the fluent solver, one must specify certain parameters and input boundary conditions. The fluid domain was chosen as water instead of air, the bottom surface was set to be a translationally moving plate in the x-direction and was set as a no-slip boundary condition, the top wall was set as a stationary wall, and the side walls were set as translationally periodic boundary conditions in order to get a velocity profile that is a function of time and position in the y-direction only. This setup allows us to compare our simulation results to the documented analytical solutions. In literature, the parallel plate is setup is as a semi-infinite domain with one-dimensional velocity (function of only 1 cartesian coordinate), in order to ignore edge effects and

simplify the solution. This setup gives an excellent approximation for the full 3D parallel plate. The solver setup differs slightly when doing a steady state versus a time-dependent run.

2.2.3.1 Steady State Solver

For steady state cases, the solver was a pressure-based solver, Absolute velocity formulation, and steady time. As the cases were run at low reynolds numbers, the model used was laminar. The solution methods were: SIMPLE Scheme Pressure-Velocity Coupling, Least Squares Cell Based Gradient Spatial Discretization, Second Order Pressure Spatial Discretization, and Second Order Upwind Momentum Spatial Discretization. Moreover, the velocity of the plate was set as a constant translational value in m/s with a translation vector of $(1, 0, 0)$. The cases were initialized using hyper-initialization as there are no inlets or outlets, and the number of iterations was chosen to be equal to or larger than 5000 iterations. This number of iterations is not necessarily the only one to use, but steady convergence of the residuals is seen for the velocity components as well as the continuity equation. The residuals are calculated by fluent using the imbalances from the conservation equation. These imbalances decay and then stop changing. With a perfect precision computer, one can get values of residuals that are 0. However, with normal computers, residuals decay to very small values 10^{-10}. When the residuals level out, at values on the order of 10^{-8} to 10^{-12}, then the solution is stable and accurate. The following figure shows an excellent convergence for the residual values yielding a stable solution:

As seen from Figure 2.4, the residuals have reached a steady value where they dont change no matter how many iterations one adds. The solution is thus stable.

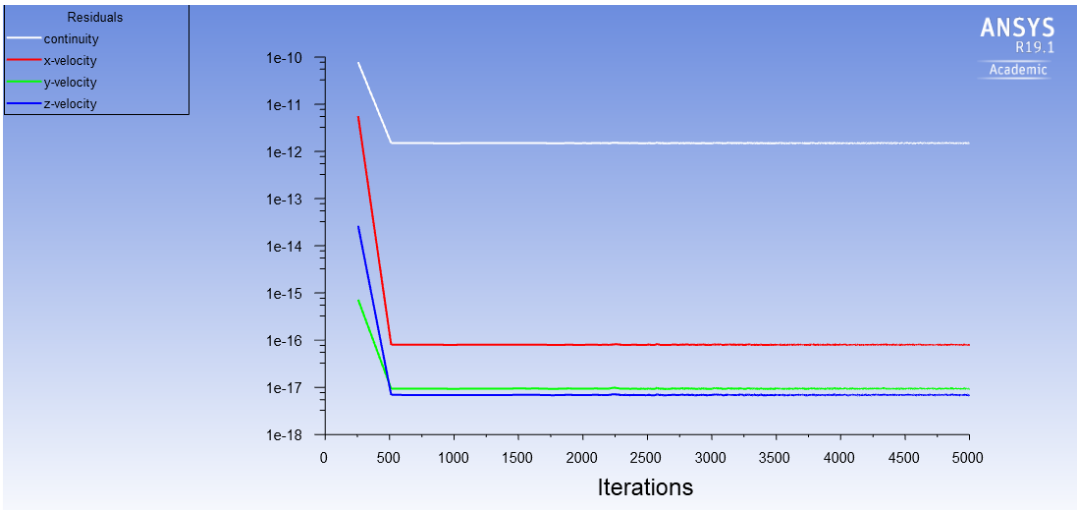

Figure 2.4: Residuals as a function of number of iterations

2.2.3.2 Transient State Solver

The setup for transient state cases is mostly the same as the steady state case. However, the time must be indicated as transient. Default settings were used for the solution methods: SIMPLE Scheme Pressure-Velocity Coupling, Least Squares Cell Based Gradient, Second Order Pressure, and Second Order Upwind Momentum Spatial Discretization. Moreover, First Order Implicit Transient Formulation was used. The rotational/translational velocities were specified using two ways:

- User-Defined-Functions (UDFs): Fluent allows the user to input the velocity of a boundary condition as a UDF written in C programming language. A UDF was used to oscillate the plate sinusoidally.

- Multiple runs: For the transient state cases, each case was broken down into two sub-runs translation period and a stopping period. After each sub-run, the data was saved and used as initial data for the sub-run after,

and so on. This method was used due to the difficulty of writing a piece-wise step-function as a UDF in C programming language.

After specifying the translational velocity, one must choose appropriate time step and iteration. This choice becomes critical when computational limitations exist, and issues such as bad convergence or unstable solutions arise when choosing a large time step. In our case, we utilized the OSCER supercomputer resources at the University of Oklahoma and were able to choose time steps as small as 10^{-4} seconds with no issues or excessive computational time. (The code and detailed explanation about the utilization of the Slurm can be found in Appendix B.)

2.2.4 Model Validation

In order to validate the model, simulation results for the velocity as a function of position and time were compared to these predicted by literature. As we want to be consistent with the cone and plate device, the height between the moving and stationary plates corresponds to the distance between a point on the cone (located at half way the radius of the cone) and the plate. The linear velocity was then calculated at that point and used for the translational velocity of the plate. These numbers can be found in Section 3.1.

The velocity of the fluid as a function of time due to a moving plate in a parallel plate geometry is given by (Bird et al. 2007):

$$\phi(\boldsymbol{\eta}, \boldsymbol{\tau}) = (1 - \boldsymbol{\eta}) - \sum_{n=1}^{\infty} \left(\frac{2}{n\pi} \right) \exp\left(-n^2\pi^2\tau\right) \sin n\pi\eta \tag{2.1}$$

Where ϕ is the dimensionless velocity, η is the dimensionless height, and τ is the dimensionless time. Equation 2.1 has two terms, a steady term and a transient term. The first term, (1-$\boldsymbol{\eta}$), is the solution to the steady state solution of

the moving plate. The second term, $(\sum_{n=1}^{\infty}\left(\frac{2}{n\pi}\right)\exp\left(-n^2\pi^2\tau\right)\sin n\pi\eta)$, is the transient term which vanishes as time increases.

The following graph shows both simulation and literature results:
In essence, this is a startup flow problem where the velocity profile develops over time until it reaches steady state (for the complete derivation of the equations, see Appendix B.) When calculating the velocity using Equation 2.1, 30 terms were used for the summation. This number of terms was enough as the contribution of each term decreases as time increases.

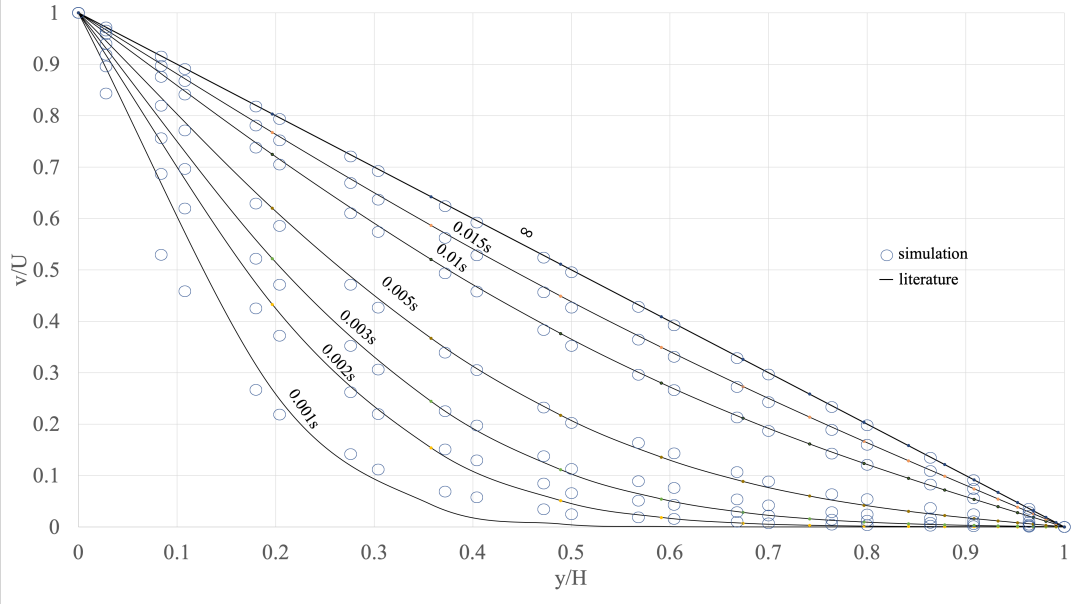

Figure 2.5: Velocity as a function of position and time

From Figure 2.5, one can see that there are differences between the simulation and literature results. CFD results are not as accurate as the analytical solution give by Bird et al. (2007), especially at lower times. The difference in velocity values at 0.001 seconds between the literature and simulation results is larger than 100 percent at certain y/H values. However, as the time increases, the simulation results are closer to the analytical values. For instance, at time

0.015 seconds, the difference between the simulation and analytical velocity values are less than 3 percent. Despite the differences between the analytical and simulation results at small time values, we can still safely conclude that our model yields accurate results and will be valid to use for transient runs.

2.3 Cone and Plate Device (CPD)

After setting up the case of the parallel plate where literature solutions exist for both the steady case and time dependent case, the cone and plate geometry was simulated:

2.3.1 Building the Geometry

Figure 2.6 below shows a diagram of the cone and plate device used in experiments (Kouzbari et al. 2019):

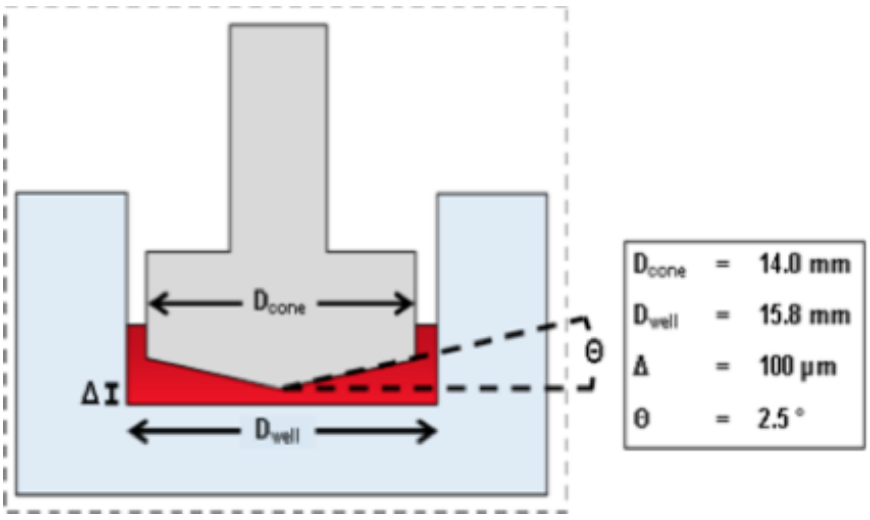

Figure 2.6: Diagram of the Cone and Plate device used in experiment

A 2D sketch with the proper dimensions was constructed (Figure 2.7). The 2D sketch is then revolved around the Y-axis to produce a full 3D model of

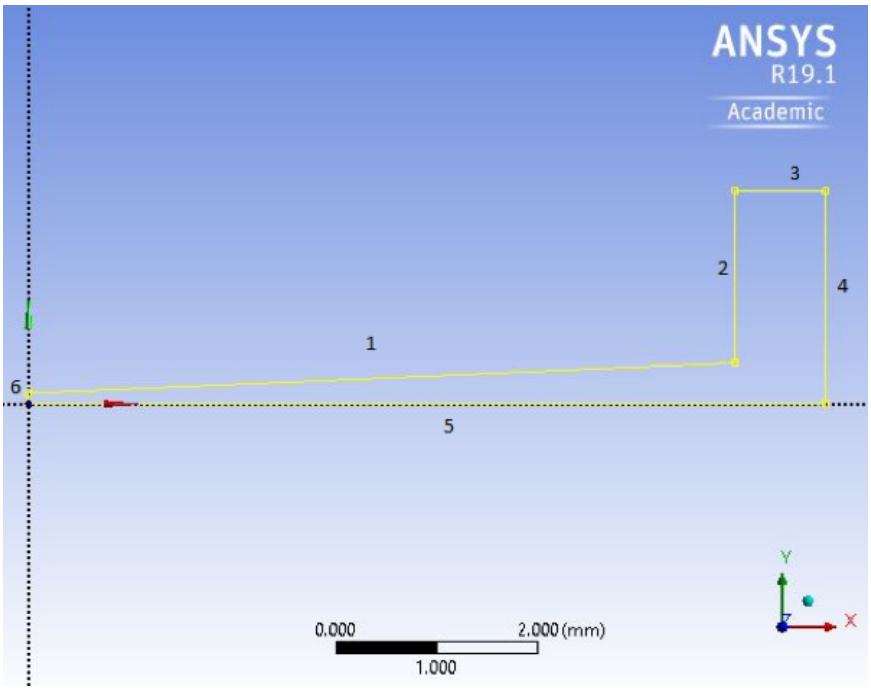

Figure 2.7: 2D sketch of the fluid domain

the fluid inside the CPD chamber (Figure 2.8). Table 2.1 lists the different boundary conditions used for each face in our geometry.

Face	Boundary condition
Cone	No slip, rotational about Y-axis
Free surface	Symmetry wall
Side wall	No slip, stationary
Plate	No slip, stationary

Table 2.1: Boundary conditions for CPD

2.3.2 Constructing the Mesh

Fluent mesh modeler was used to create a mesh for our domain (Figure 2.9):

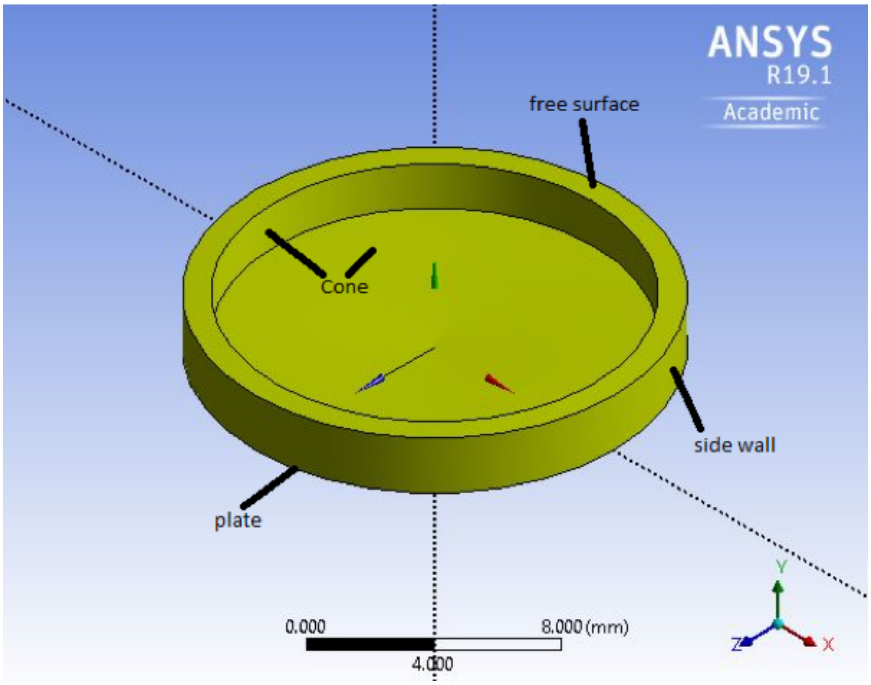

Figure 2.8: 3D model of the fluid domain

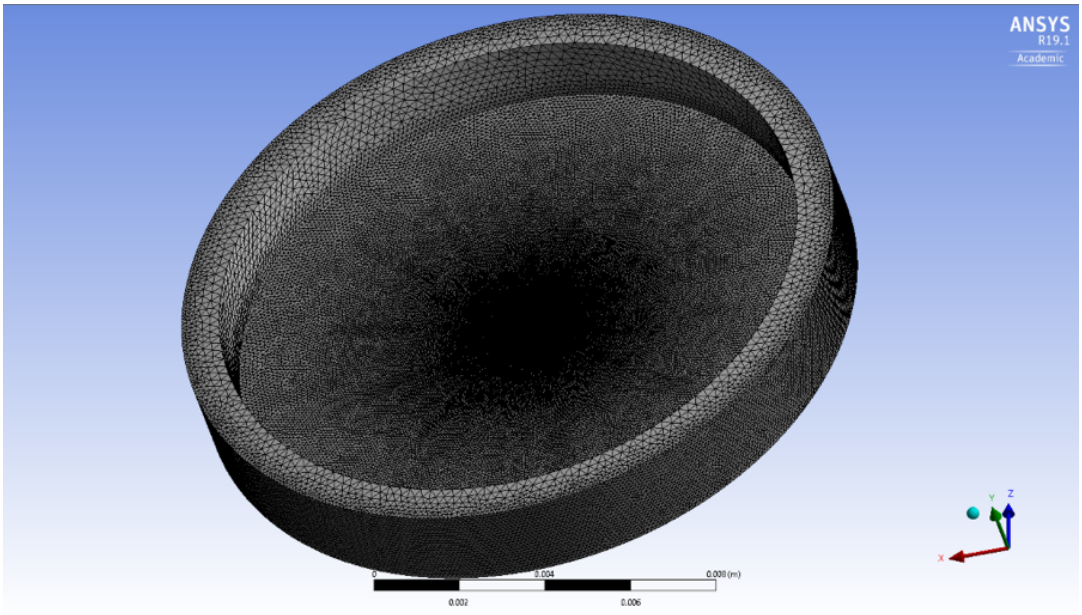

Figure 2.9: 3D sketch of the fluid domain

Number of Mesh elements*1000	Volume average shear rate (1/s)
10	215.14
300	224.052
500	225.94
863	225.75
1600	224.94
2700	226.15

Table 2.2: Mesh Independence Analysis

The following mesh metrics were recorded for the mesh:

- The average orthogonal quality is:0.7706, while the highest is 0.995 and the lowest is 0.2003.
- Aspect ratio: The average aspect ratio is 1.8545.

For the definition and further explanation of these metrics, the reader is referred to Appendix C.

Moreover, we performed a mesh independence analysis to ensure that our computed solution is independent of the mesh resolution. The volume averaged shear rate in the fluid is the value of interest in our investigation, therefore it was chosen for comparison. Table 2.2 lists the different meshes used. Figure 2.10 shows the volume averaged shear stress versus number of mesh elements for the five meshes used for the mesh independence analysis study. Therefore, as seen from Figure 2.10, a number of mesh elements that is larger than 500K will ensure that the solution is independent of the mesh resolution. The number of mesh elements used in our runs is $860,000$ elements. It is important to

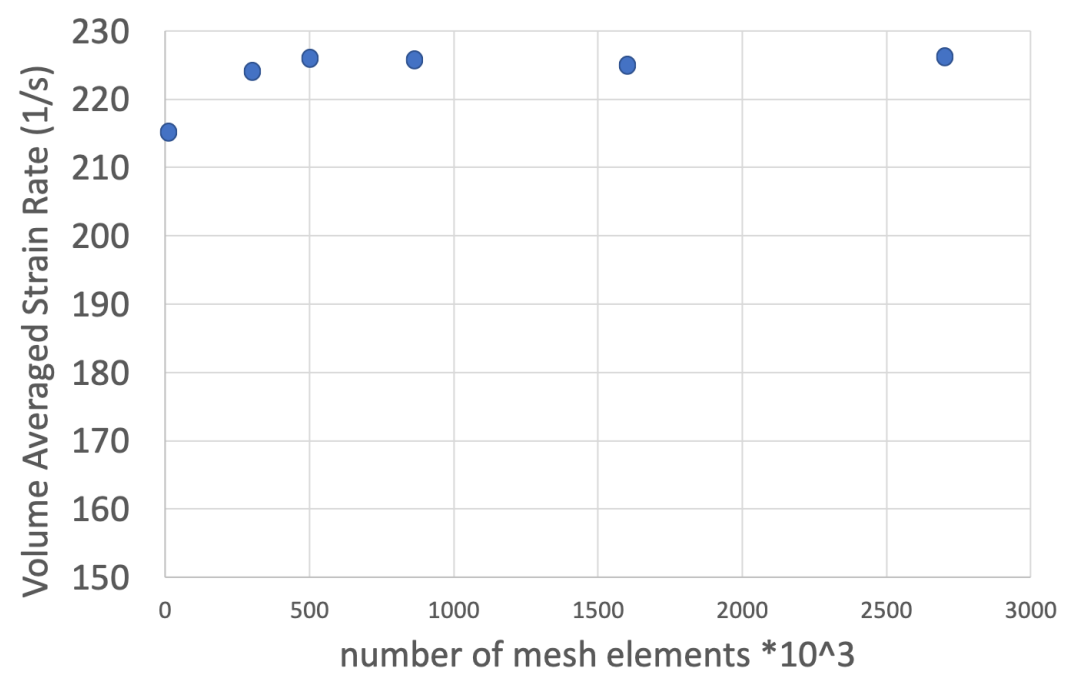

Figure 2.10: Volume average shear rate as a function of number of mesh elements

realize that even though a larger number of mesh elements might yield a more accurate solution, the computational time is significantly affected by the number of mesh elements. A larger number of elements will require a much larger computational power and more computational time. In our case, a 3D model with 860K elements was good as supercomputing resources were available.

2.3.3 Model Validation

In order to validate our model, we compared the computed shear stress profile on the surface of the plate from the simulation with that obtained from literature. Sdougos et al. (1984), performed an expansion of the Navier-stokes equations for small values of a parameter they called R. Sdogous defined R as the ratio of centrifugal forces to viscous forces:

$$R = \frac{r^2 \omega \alpha^2}{12\nu} \tag{2.2}$$

Where r is the local radius, ω is the angular velocity of the cone, α is the angle of the cone, and ν is the kinematic viscosity of the fluid. Sdougos et al. (1984) explained that the fluid shear stress, the angle of the plate-surface streamline, and the onset of turbulence are all functions of the single parameter R. For low values of R, the fluid flow is defined as a primary flow in which the entire fluid is following the motion of the cone (concentric circles) as predicted by theory. However, when the value of R is larger than 4, secondary flows appear in the fluid motion. Secondary flows are defined as minor flows which are superimposed on the primary flow. In other words, secondary flow is where the fluid is not flowing in the same direction as the majority of the fluid. Furthermore, Sdougos et al. (1984) defined the shear stress on the surface of the plate-in the limit of low rotational speeds as:

$$\tau = \mu \omega \alpha \tag{2.3}$$

This equation applies only when the cone apex is directly placed on the plate. However, when using the cone and plate device in biological applications, it is important to have the cone apex elevated a distance above the surface of the

plate in order to not damage the cells to be studied. Therefore, (Sucosky et al. 2008), modified the shear stress equation to include the effect of the gap height:

$$\tau = \mu\omega r(h_0 + r\alpha) \tag{2.4}$$

Where h_0 is the gap height between the cone apex and the surface of the plate.

The height used in the CPD used in experiments is 100 micrometers. Therefore, I simulated three different heights 1, 10, and 100 micrometers. Using equation 2.4 and from simulation, the following graph is obtained:

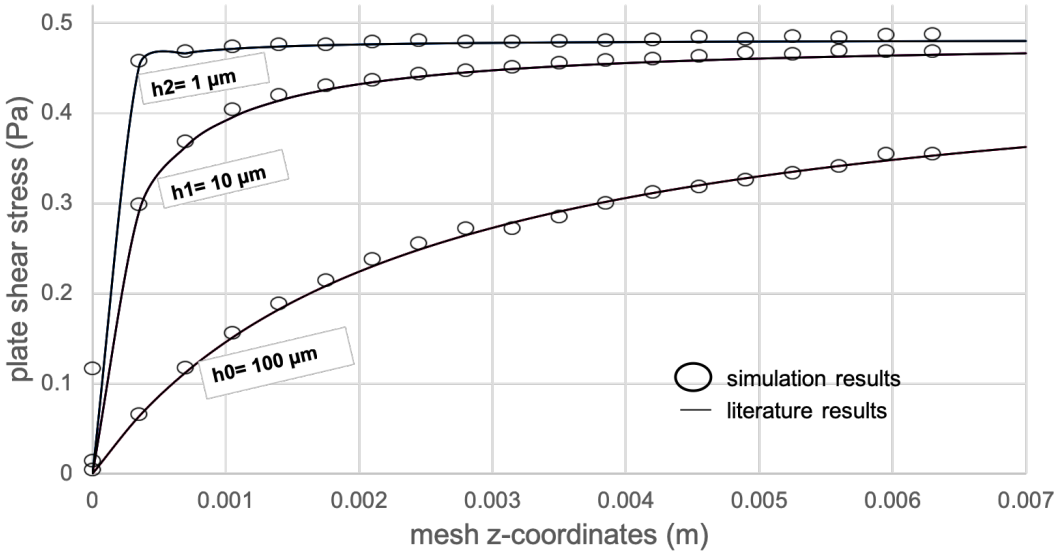

Figure 2.11: Shear stress as a function of position on the surface of the plate

Note: Literature results are calculated from Sucosky et al. (2008).

Clearly, the model succeeds in producing correct results. There is no reason why the z-coordinates were plotted instead of x-coordinates as the plate is in the XZ-plane.

Chapter 3

Results and Discussion

Our assumptions for both the parallel plate and cone and plate cases are as follows: 1- The fluid used in simulation was specified as water. This is a correct assumption as the fluid used in experiments in the cone and plate device was mainly water. 2- The distribution of TGF-β1 suspended in the fluid domain is assumed to be uniform.

3.1 Literature Review

Bi-directional shear stress is produced in a parallel plate by translating the plate in both the positive x-direction and the negative x-direction. There are multiple ways one can translate the plate in two directions, it could be done using a sinusoidal function, an abrupt stop of the plate, or a linear deceleration/acceleration of the plate. In laboratory experiments, our collaborator programmed the CPD to rotate in one direction for 0.5 seconds, spend 10 milliseconds in a linear deceleration/acceleration, then 0.5 seconds rotating in the other direction. Therefore, we use these same intervals for running the parallel plate. According to literature, as the plate spends most of its time translating (0.5 seconds) and stops for very brief time (10 milliseconds), the shear stress profile will be very similar to the steady state case. Loudon and Tordesillas (1998), explains that in the limit of small Womersley number, $W_o << 1$, the time dependent translation of

the plate can be approximated by the instantaneous boundary conditions. The Womersley number is a dimensionless group that is defined as the ratio of the unsteadiness of the flow to the viscous forces:

$$W_o = \frac{L^2 n}{\nu} \tag{3.1}$$

Where L is the maximum distance between the two plates, n is the oscillation frequency of the plate, and ν is the kinematic viscosity of the fluid. The magnitude of a dimensionless group can provide us with a sense for the relative importance of competing mechanical phenomena thereby allowing insight into some mechanical events such as laminar or turbulent behaviours (Loudon and Tordesillas 1998).

Our system has a Womersley Number of 0.1 which indicates that that the stopping period of the plate does not impact the moving fluid in the parallel plate. Hence, we predict that the time dependent flow should be well-approximated by the instantaneous boundary conditions and thus the steady state solution can be used to accurately describe the system. More importantly, this behaviour is seen only in the limit of Reynolds Number going to zero. Therefore, in this section we test this prediction by using the different modes of translating the plate and we extend that to our cone in the CPD. We predict that the shear stress profile in the time-dependent translation of the plate to be the same as that in the steady state case. Moreover, we expect that both the linear deceleration/acceleration and the abrupt stop will yield the same shear stress profile as they have the same Womersley Number. With the previous discussion in mind, the following results are obtained for all three modes of rotation: linear deceleration/acceleration, abrupt stop, and sinusoidal rotation. All of this discussion applies to the case of the cone and plate device as well. In our runs we

use a value of 200 RPM for the rotation of the cone, which yields a shear rate value of 480 s^{-1} which falls in the physiologic range between (0-2000) s^{-1}(Yap et al. 2012).

3.2 Parallel Plate

In order to be consistent with the cone and plate, we picked a point at (r=3.5 mm) on the cone and calculated the linear velocity of the cone at that radius. The linear velocity, $V_0 = 0.073304m/s$, was used for the velocity of the moving plate, and the height between the plate and cone at that radius is $h = 0.2528mm$ was used for the distance between the two plates. We then used a cosine wave, linear deceleration/acceleration, and abrupt stopping of the plate and computed the following results:

3.2.1 Sinusoidally Oscillating Wall

In this section we show the results of the volume averaged shear rate as a function of time for the case of an oscillating plate. As expected, the behavior follows the sinusoidal velocity function. Moreover, the minimum and maximum values of the strain rate in the fluid inside the parallel plate were computed as 106.2 s^{-1} and 120.2 s^{-1}. Using the iso-value function in Fluent, cells that have a value that falls in between the minimum and maximum values were marked and separated from the fluid domain. It was then computed that 98 percent of the fluid domain has a value of shear rate that is higher than 107 and less than 120. This means that there are no areas of significantly high shear rates in the fluid. For clarity purposes the shear rate values were divided by the highest shear rate value.

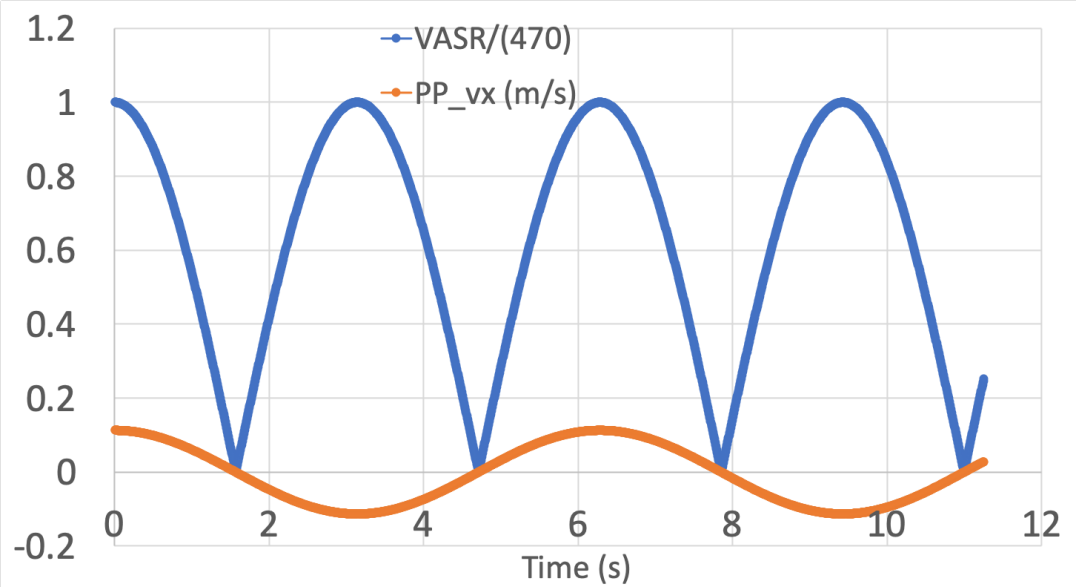

Figure 3.1: Volume averaged shear rate (VASR) as a function of time-sinusoidal oscillation

3.2.2 Linear Deceleration/Acceleration

After translating the moving plate in the +x direction for 0.5 seconds, we had the plate decelerate from V_0 to zero then re-accelerate back to -V_0 in a period of 10 milliseconds, then we let the plate translate at -V_0 for 0.5 seconds. The volume averaged shear rate profile as a function of time is seen in Figure 3.2. For clarity purposes when plotting both the velocity and volume averaged shear rate, the latter was divided by the constant volume averaged shear rate from the first 0.5 seconds of translation:

Figure 3.3 shows a closer view on the stopping period: As seen from Figures 3.2 and 3.3, the volume averaged shear rate is constant for the first 0.5 seconds of the run where the velocity of the plate is constant at V_0. Whenever the plate starts in the stopping period of linearly decelerating to zero then accelerating back to -V_0, there is an increase in the value of the volume averaged shear rate

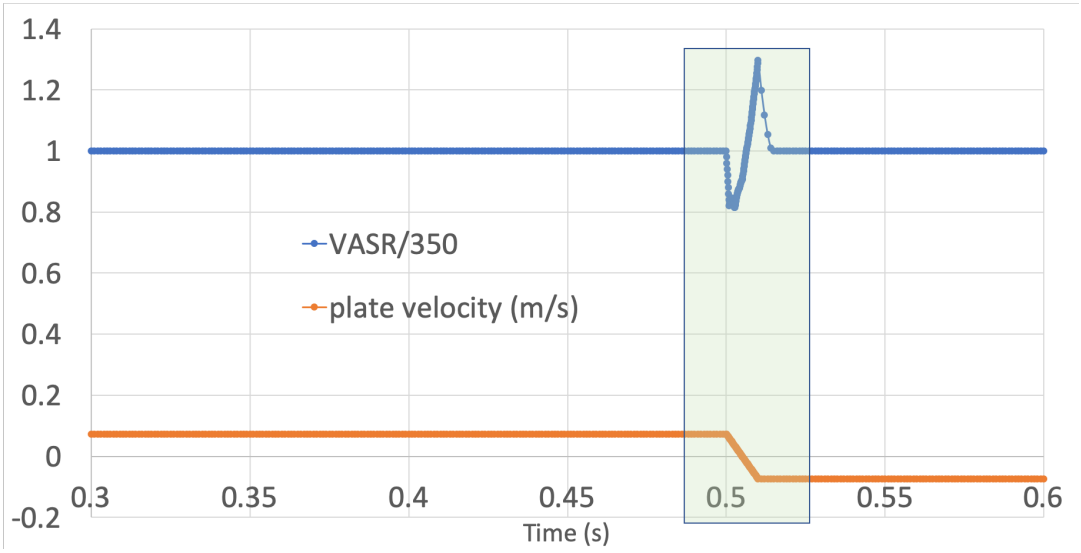

Figure 3.2: Volume averaged shear rate as a function of time-linear stopping

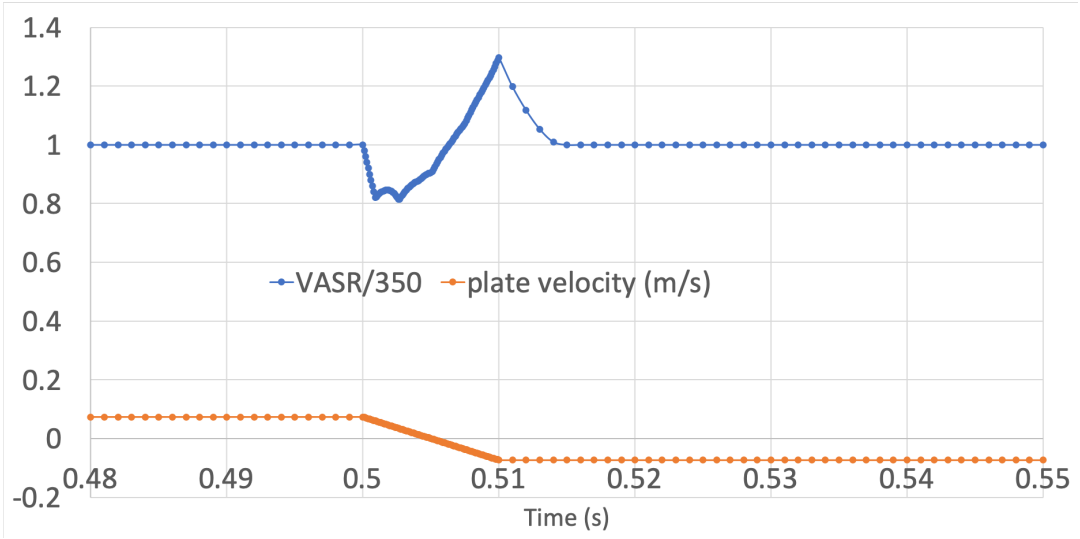

Figure 3.3: Closer view on the volume averaged shear rate profile-linear stopping

by 30 percent. In Figure 3.3, there is a section of the graph (a small hump) where the volume averaged shear rate shows an increase and a decrease by 3 percent during the decelerating period. We believe this is due to round off error when Fluent reads the User Defined Function for the velocity during the linear deceleration/acceleration. Using the iso-value function in fluent, the minimum

and maximum values of shear rate were computed to be 7 s^{-1} and 750 s^{-1}. Unlike the case of the sinusoidal oscillation of the plate we find a large disparity between the minimum and maximum strain rate values. The average value of the strain rate was 250 s^{-1} during the first 0.5 seconds of rotation while at the end of the stopping period, the volume averaged shear rate was 380 s^{-1}. This means that regions of shear rate higher than the average exist in our domain. At the end of our stopping period, the volume of cells that have a strain rate value that is between 380 s^{-1} and 750 s^{-1} constitutes 20 percent of the total volume of the fluid.

3.2.3 Abrupt Stopping

In this mode of translation, the plate was moved for 0.5 seconds in the +x-direction at V_0, stopped for 10 milliseconds at $v = 0 \quad m/s$, then moved in the (-)x-direction at velocity V_0. Simulation results yielded the following results:

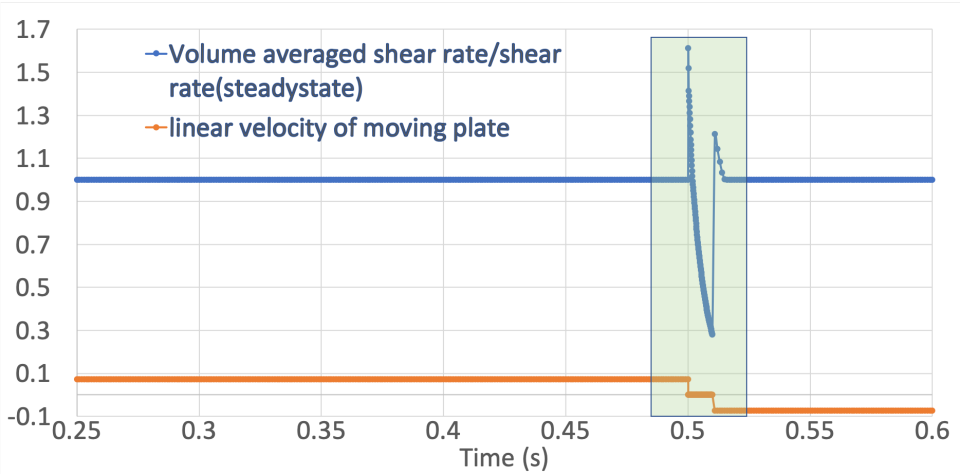

Figure 3.4: Scaled volume averaged shear rate as a function of time-Abrupt stop

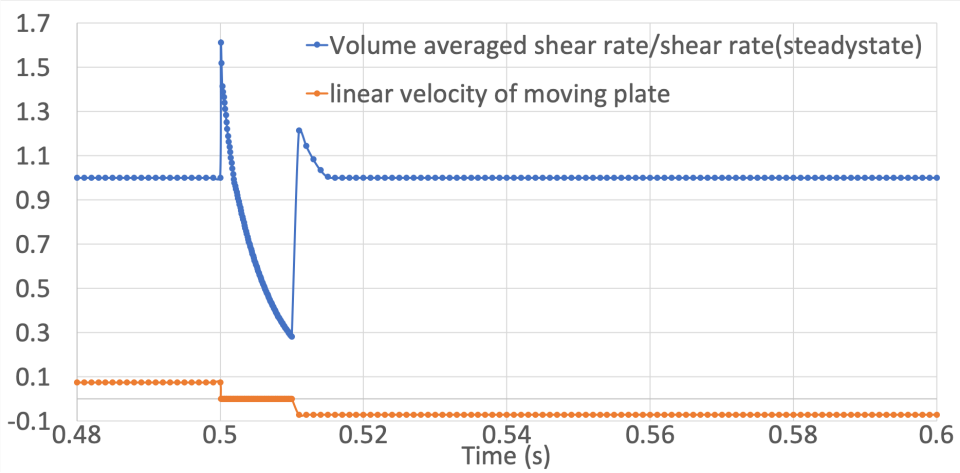

Figure 3.5: Closer view on the volume averaged shear rate-Abrupt stop

As seen in Figures 3.4 and 3.5, the volume averaged shear rate is constant throughout the first 0.5 seconds of translation. When the plate is abruptly stopped for 10 milliseconds from 0.5-0.51 seconds, we see a spike in the shear rate, that is 1.6 times higher than that seen for the first 0.5 seconds and the spike then decreases rapidly by 82 percent in value over the stopping period. Once the plate is started to translate again, the volume averaged shear rate shows another spike that is 1.2 times higher than the average value seen for the first 0.5 seconds of translation. This spike decreases back to the constant average value after 0.006 seconds from the start of the translation. Using the Iso-value function in Fluent, at the end of the stopping period, 0.51 seconds, the volume averaged shear rate value is about 75 s^{-1} while the maximum and minimum values of shear rate are 130 s^{-1} and 7 s^{-1}, respectively. The volume of fluid that is experiencing shear rate values between 75 and 130 s^{-1} is about 65 percent of the total volume of the fluid.

3.3 Cone and Plate

In this section we use the same modes of plate translation to rotate our cone. We then compute the volume averaged shear rate profiles and investigate whether regions of elevated shear rates exist in our domain or not. For the sinusoidal rotation of the cone we ensured that the average velocity of the cone rotation was the same as that used in the other two modes of rotation. We did that by equating the areas under the curve for the sinusoidal velocity function with the area under the curve for the abrupt change and adjusted the amplitude of our cosine wave accordingly.

3.3.1 Sinusoidal Rotation

In this case, the resultant shear rate profile is expected to follow the same oscillatory behavior as the cone. The shear rate and the velocity profiles are expected to be in phase until large values of the Womersley number ($W_o > 10.$) We hypothesized that a phase lag will be noticeable once the fluid is in the turbulent regime due to the significant effect of secondary flows at such Reynolds Numbers ($R > 4$, for the cone and plate device.). The following figure shows the volume averaged shear rate profile as a function of time for the low Re number case (Figure 3.6, Re = 0.25): The lag in time is zero between the maximum value of the strain rate and the minimum value of the rotational velocity. Now, when looking at the case of high Re number (Figure 3.7, Re = 4.5), a lag of 0.05 is calculated between the time of the maximum value of shear rate and minimum value of rotational velocity (Cannot be seen in figure due to large difference in values between the shear rate and rotational velocity). The following figure shows the volume averaged shear rate profile as a function of time for the high

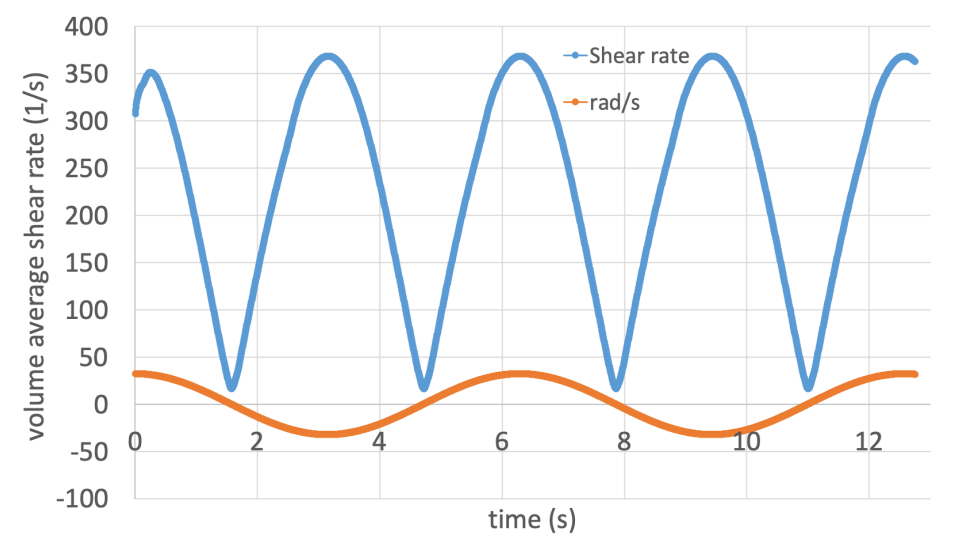

Figure 3.6: Volume averaged shear rate as a function of time-sinusoidal rotation-low Re

Re number case:

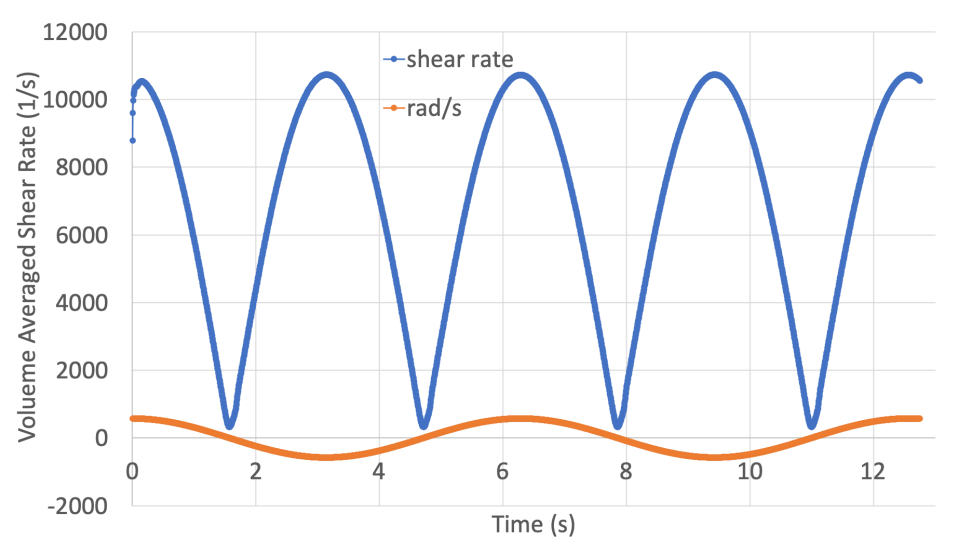

Figure 3.7: Volume averaged shear rate as a function of time-sinusoidal rotation-high Re

Despite the drastic change in the rotational velocity between both cases (low

Re, 30 rad/s and high Re, 576 rad/s,) the lag between the peak of the shear rate and the trough of the velocity profile is only 0.05 seconds which is 0.4 percent of the time of two full cycles in rotation of the cone. Clearly, such a low phase shift will not have a significant impact on the fluid flow inside the CPD. This gives us the idea that phase-shift expected between the shear stress and velocity profile is not a function of the amplitude of the velocity (Reynolds Number), but rather a function of the oscillation frequency and gap distance (in the Womersley Number).

Using the iso-value function in Fluent, the minimum and maximum values of shear rate at the end of the sinusoidal rotation are 0.6 s^{-1} and 1690 s^{-1}. The difference between minimum and maximum values is quite large and our volume averaged shear rate at the end of the rotation is about 350 s^{-1}. Therefore, we defined high shear rate regions as the cells with a shear rate values between 700 s^{-1} and 1690 s^{-1}. The volume of the fluid that exhibited shear rate values that fall in this range was calculated to be 5 percent of the total volume of the fluid. This follows our prediction that regions of high shear rates are small in the case of sinusoidal rotation.

3.3.2 Linear Deceleration/Acceleration

In this mode of rotation, the cone was rotated at 200 RPM in one direction for 0.5 seconds, then a linear deceleration to zero and acceleration to 200 RPM in the opposite direction over a period of 10 milliseconds. The cone was then rotated at -200 RPM for 0.5 seconds. Two complete cycles where simulated, and the following volume averaged shear rate profile as a function of time for one cycle is shown in Figures 3.8 and 3.9: The first 0.5 seconds, the shear rate profile is constant, similar to the steady state case. During the stopping period,

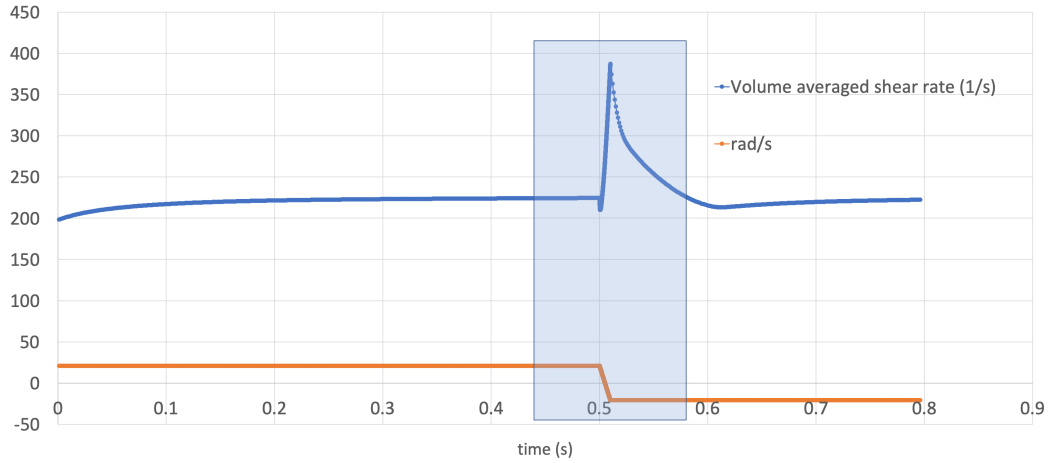

Figure 3.8: Volume averaged shear rate as a function of time during the linear deceleration/acceleration

a slight decrease of about 6 percent over a period of 0.00062 seconds is seen, and then a spike in the shear rate is seen which is 1.7x the average shear rate. When the cone starts rotating in the opposite direction, a decrease in the shear rate occurs until it reaches the steady state value. When zooming in on the blue box in Figure 3.8 one can observe closely the behavior during the stopping period:

At the end of the stopping period, the minimum and maximum shear rate values are 0.6 s^{-1} and 3973 s^{-1}, while the volume averaged shear rate at that point is 380 s^{-1}. We calculated the volume of fluid that experiences shear rate values between 760 s^{-1} (2x the average) and 3973 s^{-1} to be 13 percent of the fluid domain. This indicates that there is a portion of the fluid that is experiencing elevated shear rate values at the end of the stopping period. Therefore, despite the Reynolds Number being 0.16, which suggests that inertial effects are negligible, we still observe the inertial effects of the fluid due to cone deceleration/acceleration

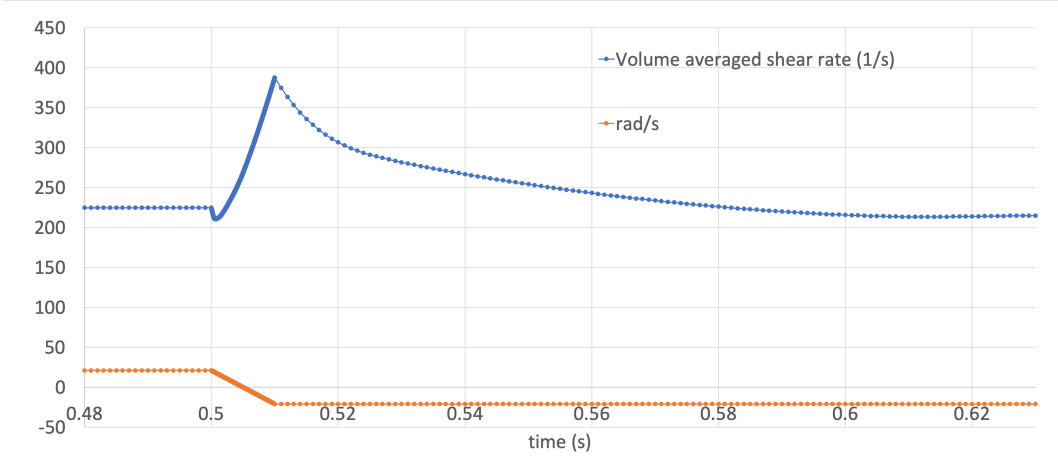

Figure 3.9: Closer view on the stopping period during the linear deceleration/acceleration

As the Reynolds Number approaches zero, one expects the fluid flow to be mainly governed by primary flow. In our case, the primary flow is in the tangential direction due to the rotation of the cone. Figure 3.10 shows the different velocity components that exist in our system. The axial and radial velocity components are expected to be zero or very low compared to the tangential velocity component, as predicted by literature (Sdougos et al. 1984). In order to check that this is the case in our model, we looked at the contours of velocity during the stopping period. The following three contours show the tangential, radial, and axial velocity at time 0.501 seconds where the cone velocity has decreased from 200 RPM to 196 RPM:

The red area on the contours is where the maximum value of the respective velocity component exists. In the case of the tangential velocity the maximum value is $1.33 * 10^{-1} m/s$, and for the radial and axial velocities, the maximum values are $4.71 * 10^{-3} m/s$, and $6.3 * 10^{-3} m/s$, respectively. The maximum values of the radial and axial velocities are only 3.46 percent and 4.74 percent of

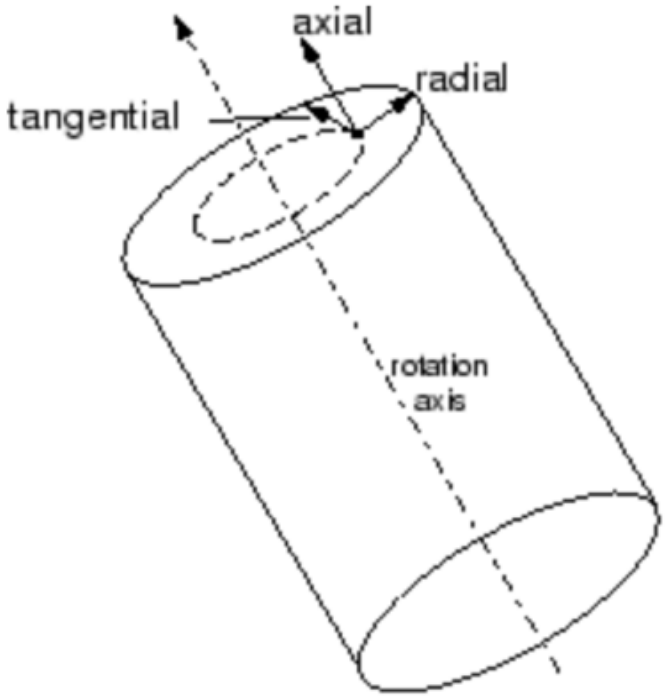

Figure 3.10: Velocity components directions as defined in Fluent

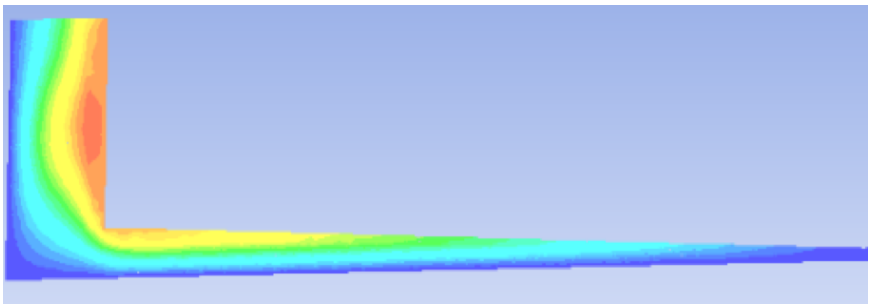

Figure 3.11: Tangential velocity contours at time 0.501 seconds

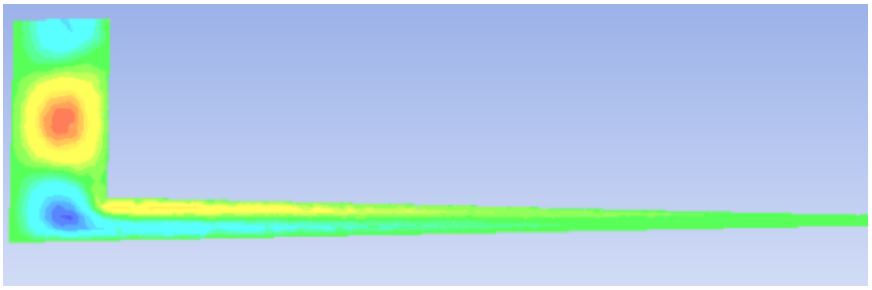

Figure 3.12: Radial velocity contours at time 0.501 seconds

Figure 3.13: Axial velocity contours at time 0.501 seconds

the tangential velocity at time 0.501 seconds. As the cone continues during the stopping period, the relative magnitudes of the maximum values of the axial and radial velocities compared to the tangential velocity do not show significant changes as can be seen from Tables 3.1 and 3.2. Although these tables show that secondary flows exist, unlike what is predicted by Sdougos et al. (1984), these secondary flows are too small to have an effect.

Over the stopping period, the maximum value of the tangential velocity decreases by 13 percent in value, while the maximum values of the radial and axial velocities increase by about 1 percent and 2 percent, respectively. Moreover, the maximum values of the radial and axial velocities are less than 10 percent in value compared to the tangential velocity and therefore we neglect any effect they might have on the fluid flow.

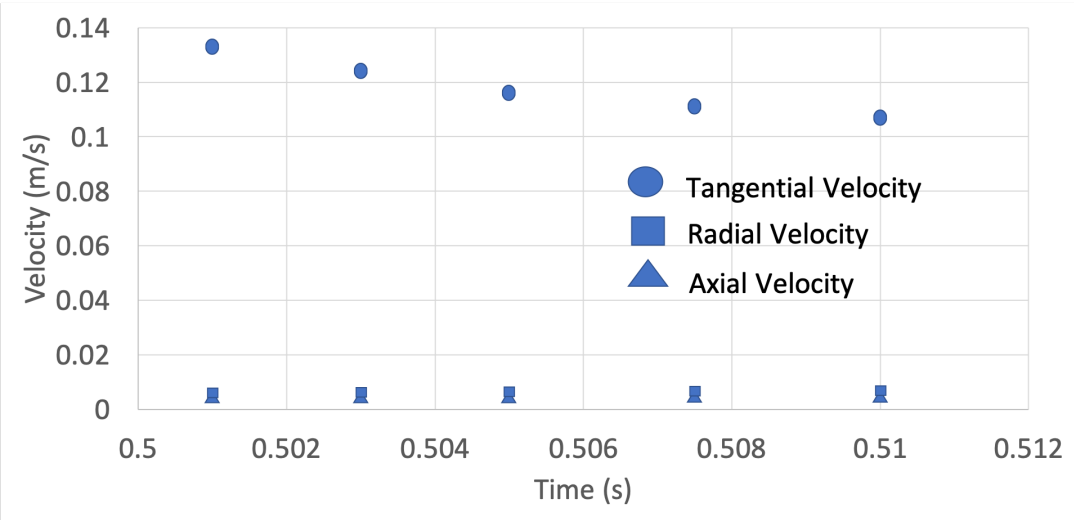

Figure 3.14: Tangential, radial, and axial velocity magnitudes as a function of time over the stopping period

Time (s)	Radial velocity compared to tangential velocity (percent)
0.501	3.45
0.503	3.82
0.505	4.20
0.5075	4.50
0.51	4.72

Table 3.1: Radial velocity values compared to tangential velocity during the stopping period-linear stopping

Time (s)	Axial velocity compared to tangential velocity (percent)
0.501	4.74
0.503	5.11
0.505	5.66
0.5075	6.23
0.51	6.65

Table 3.2: Axial velocity values compared to tangential velocity during the stopping period-linear stopping

3.3.3 Abrupt Stopping

The cone is rotated at 200 RPM in one direction for 0.5 seconds, stopped at 0 RPM for 10 milliseconds, then rotated back in the opposite direction at 200 RPM. Simulation results yielded the following volume averaged shear stress profile for the abrupt stop method:

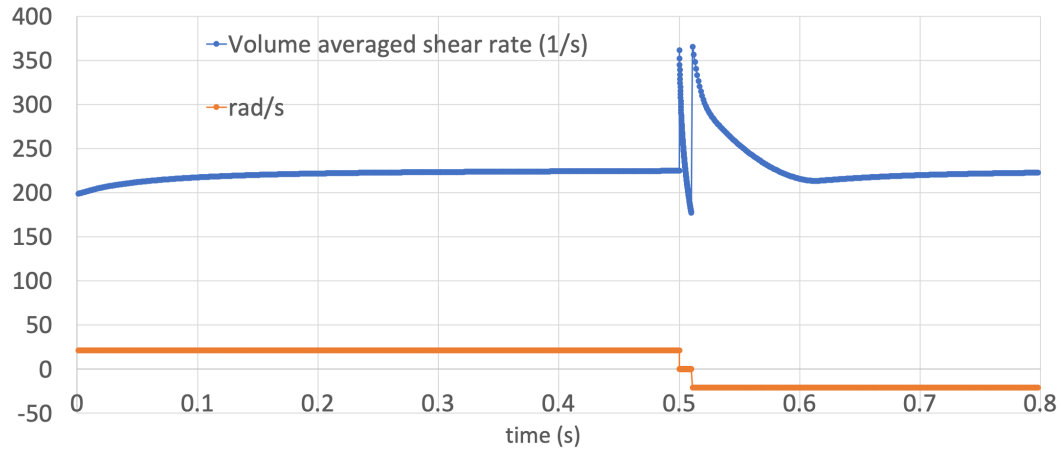

Figure 3.15: Volume averaged shear rate as a function of time-Abrupt Stop

When zooming in on the stopping period in Figure 3.15, one can observe the the shear rate profile closely:

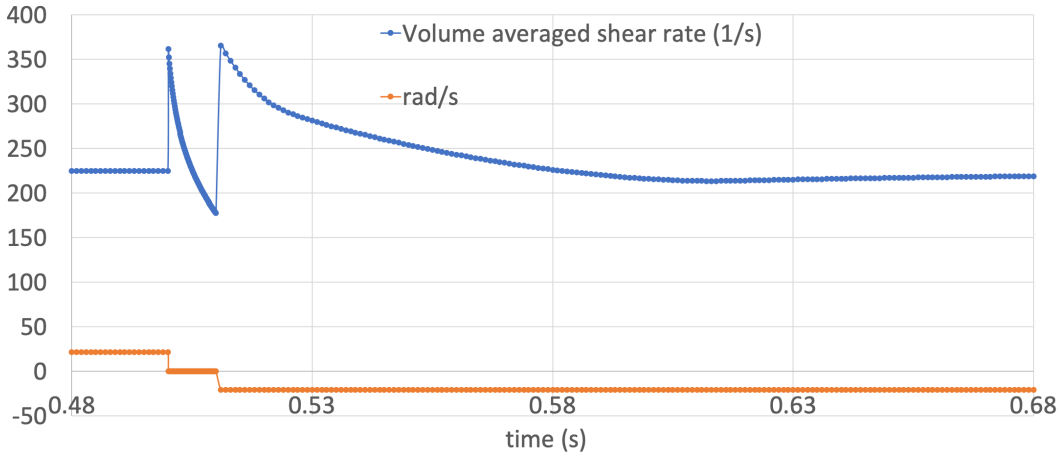

Figure 3.16: Closer view on the stopping period during the abrupt stop

The first 0.5 seconds of the run, the volume averaged shear rate values are the same as that seen in Figure 3.8 for the linear deceleration/acceleration stopping. The abrupt stopping, however, results in two peaks in the volume averaged shear stress profile. The first peak occurs when the cone is stopped (RPM drops from 200 to 0), while the second peak occurs upon accelerating the cone from 0 RPM

to 200 RPM. At the end of the abrupt stop, the minimum and maximum shear rate values are 0.001 s^{-1} and 963 s^{-1}, respectively. The volume averaged shear rate at the end of the stopping period is about 175 s^{-1}. Therefore, as the difference between the minimum and maximum shear rate values is quite large, we calculated the volume of fluid that is experiencing a shear rate value between 350 s^{-1} and 963 s^{-1} to be 5 percent of the total volume of the fluid.

Over the stopping period, the maximum value of the tangential velocity decreases by 17 percent, while the radial and axial velocities both increase by less than 1 percent. The following figure shows the maximum values of each component during the stopping period:

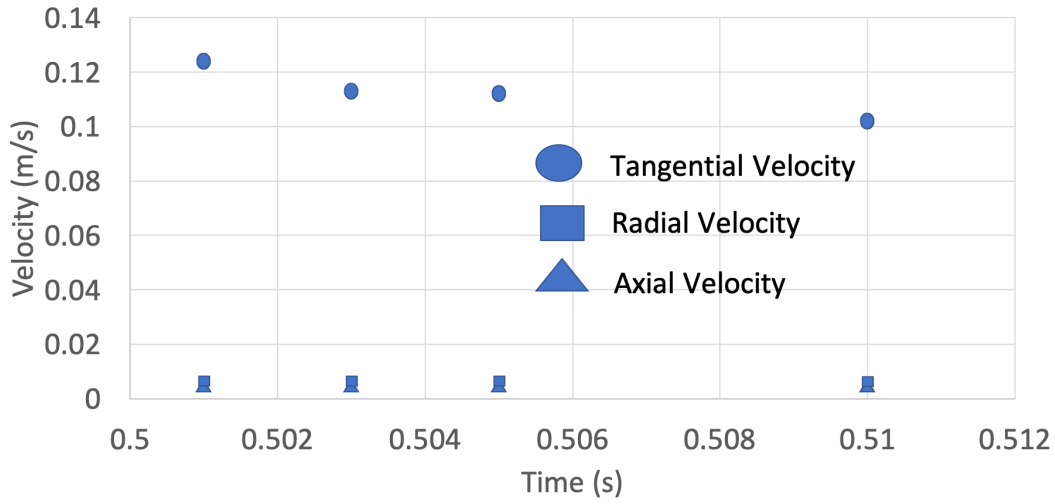

Figure 3.17: Tangential, radial, and axial velocity magnitudes as a function of time over the abrupt stopping period

Tables 3.3 and 3.4 show the relative magnitudes of the maximum values of the radial and axial velocities compared to the maximum value of the tangential velocity at four different points in time during the stopping period:

Time (s)	Radial velocity compared to tangential velocity (percent)
0.501	3.88
0.503	4.36
0.505	4.39
0.51	4.72

Table 3.3: Radial velocity values compared to tangential velocity during the stopping period

Time (s)	Axial velocity compared to tangential velocity (percent)
0.501	5.32
0.503	5.84
0.505	5.88
0.51	6.25

Table 3.4: Axial velocity values compared to tangential velocity during the stopping period

Chapter 4

Conclusion and Future Work

In this thesis we constructed and validated a parallel plate geometry were one plate is moving and the other is stationary. We validated the parallel plate model by computing the velocity as a function of position from our model at different times and compared these velocity values to that predicted by literature. We saw that the CFD solution has limitations at predicting the velocity at low time steps (0.0001 seconds). Moreover, we showed that different ways of creating oscillatory shear in the fluid between the two plates yield different volume averaged shear rate profiles and result in different regions of elevated shear rates. For the cone and plate device, we validated the model by comparing plate shear stress computed from simulation to that calculated from literature. We then used the same three modes used in the parallel plate case to create oscillatory shear in the cone and plate device. We saw similar trends in the volume averaged shear rate profiles for both geometries. We further investigated the secondary flows in our domain and showed that the axial and radial velocities are negligible in value compared to the tangential velocity.

These results signify the distinct differences between these modes of creating oscillatory shear and the importance of correctly understanding the time dependence of the shear rate in the biological environment. Each one of these modes, when used in a cone and plate device, will have different effect on the activation of TGF-β1. This indicates that understanding the mechanical environment

inside the heart valve is very important for understanding the mechanism by which TGF-β contributes to the progression of CAVD. Until now, there are no ways of getting high resolution images of the heart valve that would help us capture the correct geometry of the valve as a function of time. We are hopeful that in the near future we will be able to create 3D geometry of the heart valve, capture the changes in the geometry during systole and diastole, and investigate the sensitivity of the blood flow to the boundary conditions.

Reference List

Benjamin, E. J., S. S. Virani, C. W. Callaway, A. M. Chamberlain, A. R. Chang, S. Cheng, S. E. Chiuve, M. Cushman, F. N. Delling, R. Deo, et al., 2018: Heart disease and stroke statistics2018 update: a report from the american heart association. *Circulation*, **137**, e67–e492.

Bird, R. B., W. E. Stewart, and E. N. Lightfoot, 2007: *Transport phenomena*. John Wiley & Sons.

Chester, A. H., I. El-Hamamsy, J. T. Butcher, N. Latif, S. Bertazzo, and M. H. Yacoub, 2014: The living aortic valve: From molecules to function. *Global Cardiology Science and Practice*, 11.

Dewey, C., S. Bussolari, M. Gimbrone, and P. F. Davies, 1981: The dynamic response of vascular endothelial cells to fluid shear stress. *Journal of biomechanical engineering*, **103**, 177–185.

Esmerats, J. F., N. Villa-Roel, S. Kumar, L. Gu, M. T. Salim, M. Ohh, W. R. Taylor, R. M. Nerem, A. P. Yoganathan, and H. Jo, 2019: Disturbed flow increases ube2c (ubiquitin e2 ligase c) via loss of mir-483-3p, inducing aortic valve calcification by the hif-1α (hypoxia-inducible factor-1α) pathway in endothelial cells. *Arteriosclerosis, thrombosis, and vascular biology*, ATVBAHA118312233–ATVBAHA118312233.

Fernández Esmerats, J., J. Heath, and H. Jo, 2016: Shear-sensitive genes in aortic valve endothelium. *Antioxidants & redox signaling*, **25**, 401–414.

Kouzbari, K., M. R. Hossan, J. H. Arrizabalaga, R. Varshney, A. D. Simmons, S. Gostynska, M. U. Nollert, and J. Ahamed, 2019: Oscillatory shear potentiates latent tgf-β1 activation more than steady shear as demonstrated by a novel force generator. *Scientific Reports*, **9**, 6065.

Loudon, C. and A. Tordesillas, 1998: The use of the dimensionless womersley number to characterize the unsteady nature of internal flow. *Journal of theoretical biology*, **191**, 63–78.

McKinley, M. P., V. D. O'loughlin, E. Pennefather-O'Brien, and R. T. Harris, 2017: *Human anatomy*. McGraw-Hill Higher Education Boston, MA.

Patel, A. and A. J. Kirtane, 2016: Aortic valve stenosis. *JAMA cardiology*, **1**, 623–623.

Sdougos, H., S. Bussolari, and C. Dewey, 1984: Secondary flow and turbulence in a cone-and-plate device. *Journal of Fluid Mechanics*, **138**, 379–404.

Sucosky, P., M. Padala, A. Elhammali, K. Balachandran, H. Jo, and A. P. Yoganathan, 2008: Design of an ex vivo culture system to investigate the effects of shear stress on cardiovascular tissue. *Journal of biomechanical engineering*, **130**, 035001.

Sun, L., N. M. Rajamannan, and P. Sucosky, 2013: Defining the role of fluid shear stress in the expression of early signaling markers for calcific aortic valve disease. *PLoS One*, **8**, e84433.

Wang, W., S. Vootukuri, A. Meyer, J. Ahamed, and B. S. Coller, 2014: Association between shear stress and platelet-derived transforming growth factor-β1 release and activation in animal models of aortic valve stenosis. *Arteriosclerosis, thrombosis, and vascular biology*, **34**, 1924–1932.

Yap, C. H., N. Saikrishnan, G. Tamilselvan, and A. P. Yoganathan, 2012: Experimental measurement of dynamic fluid shear stress on the aortic surface of the aortic valve leaflet. *Biomechanics and modeling in mechanobiology*, **11**, 171–182.

Chapter 5
Appendices

5.1 Appendix A

In this appendix, the codes that were used in running the job scripts for FLUENT, are explained. The main reason behind including this section is to help serve as a reference to whomever wants to use the supercomputing resources for Fluent, found at OU. The first file is called a batch file. This batch file is set up as the following: The SBATCH commands are for the setup of the nodes that

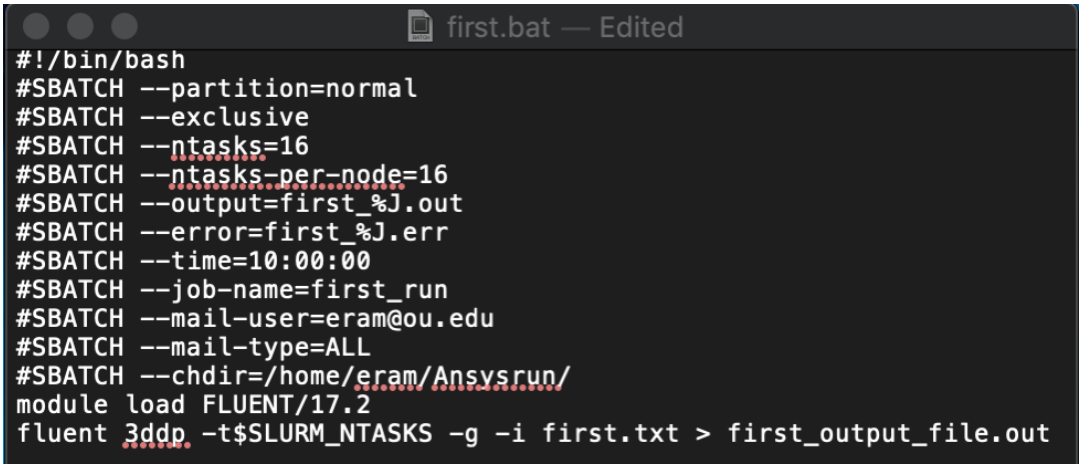

Figure 5.1: Batch File setup for Fluent on OSCER

are used in running Fluent. The first line indicates the partition type that one is intending to use. The "normal" partition is the main one and includes 20 CPU Cores. Other partitions, such as "$debug_5min$" which runs more than 20 Cores for only 5 minutes. This debug queue does not have a queue time, meaning that once a job is submitted it will be run immediately. This is a great tool for avoiding waiting 3 hours in the "normal" queue and your case failing after 3 seconds. The second line in the SBATCH command gives you an exclusive node which has 20 CPU cores. No one else can use these 20 Cores but you during the run time of your case. The third and forth lines are to determine how many CPU cores you intend on using out of the allowed number of 20. I use 16 to avoid crashing and license issue which happen at using 20 Cores. The fifth and sixth lines are for you to get output and error files that determine

reasons behind your case crashing or memory issues. The seventh line is quite important as it determines your run time. Some cases take more than 20 hours to finish, therefore, one must know roughly the run time of their setup. ***Note***: The lower your run time is, the less time you are going to spend waiting on the "normal queue".
Thus, if your case takes only one hour of run time and you put 10 hours, you will spend much more time waiting in the queue compared to your case run time. The eighth line is quite straightforward. The ninth line allows you to receive emails telling you when your time starts and ends (this is also included in the "mail type" on the tenth line.

The last line of the SBATCH commands is the working directory of your case file. This is important as one includes their case and any UDF files in the same directory file to ensure successful run of the case. The module load Fluent command is for the Slurm to start running Fluent. The last line of the Batch file is very important as the first part before the "¿" sign indicates the mode of Fluent that you are running. The command in figure 5.1 opens fluent in parallel mode at the same number of tasks allotted before in the SBATCH file. The text file "first.txt" is a file that one includes the setup of Fluent solver commands. Figure 5.2 shows an example of a text file:

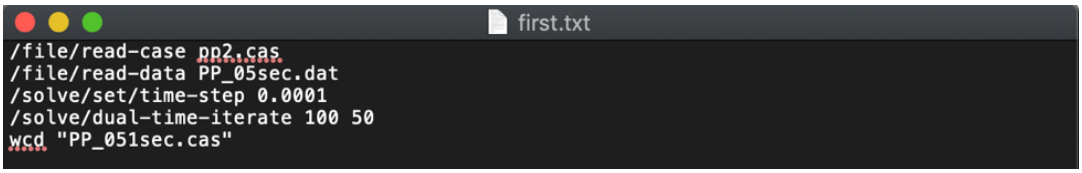

Figure 5.2: Text File setup for Fluent on OSCER-Transient State

The first two lines of the text file are to open and read the case and data files you have prepared. If you do not have a data file, you need to initiate the solver, and therefore replace the second line with ("/solve/initiate/hyb-initialization"). The third and fourth line set up the transient solver inputs: the time step, the number of time steps, and the number of iterations per time step. The last line writes the case and data files after the run is over. In the case that one is running a steady state case rather than a transient case, all what one needs to delete the third and fourth lines and include in their place a line that defines the number of iterations needed ("/solve/iterate 1000".)

5.2 Appendix B

In this section, we show the Parallel plate analytical solution. This solution is done in Bird et al. (2007) and is shown here for the reader's reference. The moving plate case is set up as the following: A liquid is bound between semi-infinite two parallel plates. One of the plates is at a distance "y=b", while the other is at distance "y = 0". At time t = 0 the wall at y = 0 is set in motion and it's desired to know the velocity as a function of position and time. There are two boundary conditions and one initial condition:

- Initial Condition: at $t \leq 0, \quad v_x = 0$ for $0 \leq y \geq b$
- Boundary Condition 1: at $y = 0, \quad v = U$ for all $t > 0$
- Boundary Condition 2: at $y = b, \quad v = 0$ for all $t > 0$

Due to the semi-infinite setup, we know that the velocity is only a function of the y-position and does not depend on the x or z directions. Therefore, using the Navier-stokes equations, the following terms remain:

$$\frac{\partial v_x}{\partial t} = \nu \frac{\partial^2 v_x}{\partial y^2} \tag{5.1}$$

As noted in BSL, it is generally more convenient to use dimensionless variables in solving fluid mechanics problems. For this case, the following dimensionless variables are introduced

$$\phi = \frac{v_x}{v_0}; \quad \eta = \frac{y}{b}; \quad \tau = \frac{\nu t}{b^2} \tag{5.2}$$

Substituting these changes in the variables in equation 5.1 above, yields the following dimensionless second order partial differential equation:

$$\frac{\partial \phi}{\partial \tau} = \frac{\partial^2 \phi}{\partial \eta^2} \tag{5.3}$$

With the transformation of the variables, one must change the initial and boundary conditions accordingly:

- Initial Condition: $\phi = 0 \quad$ at $\tau = 0$
- Boundary Condition: $\phi = 1 \quad$ at $\eta = 0$
- Boundary Condition2: $\phi = 0 \quad$ at $\eta = 1$

This problem is basically a startup flow problem, i.e. the system is going to steady state as $\tau = \infty$. Therefore, we know that at $\tau = \infty$, the differential equation in 5.3 becomes:

$$0 = \frac{d^2 \phi_\infty}{d\eta^2} \tag{5.4}$$

Using the two boundary conditions, we arrive at the following expression for the dimensionless velocity for the steady state limit:

$$\phi_\infty = 1 - \eta \tag{5.5}$$

Consequently, we can write the overall velocity profile including the transient term as the following:

$$\phi(\eta, \tau) = \phi_\infty(\eta) - \phi_t(\eta, \tau) \tag{5.6}$$

The transient term, $\phi_t(\eta, \tau)$ vanishes as time increases. substitution of equation 5.6 into 5.3, yields the following:

$$\frac{\partial \phi_t}{\partial \tau} = \frac{\partial^2 \phi_t}{\partial \eta^2} \tag{5.7}$$

with $\phi_t = \phi_\infty$ at $\tau = 0,$ and $\phi_t = 0$ at $\eta = 0$ and 1.

In order to solve equation 5.7, the method of separation of variables is used. The solution is assumed to be of the following form:

$$\phi_t = f(\eta)g(\tau) \tag{5.8}$$

substituing this form into equation 5.7 and dividing by fg:

$$\frac{1}{g}\frac{dg}{d\tau} = \frac{1}{f}\frac{d^2 f}{d\eta^2} \tag{5.9}$$

As can be seen from equation 5.9, the left hand side is only a function of τ while the right hand side is a function of η alone. This means that both sides must equal a constant. From our firm understanding of partial differential equations, we know that the constant is $-c^2$ (This constant yields the easiest mathematical expression to work with). Thus, equation 5.9 can be broken into two separate equations:

$$\frac{dg}{d\tau} = -c^2 g \tag{5.10}$$

$$\frac{d^2 f}{d\eta^2} + c^2 f = 0 \tag{5.11}$$

These two differential equations have the following solution:

$$g = Ae^{-c^2\tau} \tag{5.12}$$

$$f = B\sin c\eta + C\cos c\eta \tag{5.13}$$

Where A, B, and C are constants of integration. From the first boundary condition, we know that ϕ_∞ is zero at $\eta = 0$, therefore, f must be zero at $\eta = 0$. This can be the case only if C is equal to zero.

Using the second boundary condition, we know that ϕ_∞=0 at $\eta = 1$, which

means that f must be zero at $\eta = 0$. This can be the case if $B = 0$ or if $\sin c = 0$. If $B = 0$ then f equals zero for all cases of η. However, this is physically unacceptable and therefore, $\sin c = 0$, which means that c = 0, $\pm\pi, \pm 2\pi, \pm 3\pi, \cdots$ These eigenvalues of c can be combined as:

$$c_n = n\pi, \qquad \text{with } n = 0, \pm 1, \pm 2, \pm 3, \cdots \tag{5.14}$$

Consequently, there are a group of eigenfunctions, f_n that satisfy equation 5.11 and the boundary conditions, these can be written as:

$$f_n = B_n \sin n\pi\eta, \qquad \text{with } n = 0, \pm 1, \pm 2, \pm 3, \cdots \tag{5.15}$$

Similarly, the eigenfunctions, g_n that satisfy equation 5.10 can be written as:

$$g_n = A_n \exp\left(-n^2\pi^2\tau\right), \qquad \text{with } n = 0, \pm 1, \pm 2, \pm 3, \cdots \tag{5.16}$$

In order to satisfy the initial condition, we know that any combination of $f_n g_n$ satisfies the partial differential equation for ϕ_t in 5.7, and so will any superposition of such products. Therefore, we can write the solution of 5.7 as:

$$\phi_t = \sum_{n=-\infty}^{+\infty} D_n \exp\left(-n^2\pi^2\tau\right) \sin n\pi\eta \tag{5.17}$$

Where D_n is $A_n B_n$. In 5.17, we can change the summation lower limit as n=0 does not contribute to the summation and as $\sin(-n)\pi\eta = -\sin(+n)\pi\eta$, we can omit all the terms with negative values of n. Hence, equation 5.17 becomes:

$$\phi_t = \sum_{n=1}^{\infty} D_n \exp\left(-n^2\pi^2\tau\right) \sin n\pi\eta \tag{5.18}$$

According to the initial condition, at $\tau = 0$, we know that:

$$1 - \eta = \sum_{n=1}^{\infty} D_n \sin n\pi\eta \tag{5.19}$$

Now, we must determine all the values of D_n from 5.19 and this is done by using the orthogonality of sinusoidal functions. We first multiply both sides of equation 5.19 by $\sin m\pi\eta$, where m is an integer, and then integrate over the range from $\eta = 0$ to $\eta = 1$. Thus:

$$\int_0^1 (1 - \eta) \sin m\pi\eta d\eta = \sum_{n=1}^{\infty} D_n \int_0^1 \sin n\pi\eta \sin m\pi\eta d\eta \tag{5.20}$$

The left side gives us $1/m\pi$. For the right hand side, and using the orthogonality of sinusoidal functions, we know that the integral is zero when $n \neq m$ and 1/2 when n=m. Hence, the initial condition gives us:

$$D_m = \frac{2}{m\pi} \tag{5.21}$$

Therefore, the final expression for the dimensionless velocity profile is:

$$\phi(\boldsymbol{\eta}, \boldsymbol{\tau}) = (1 - \boldsymbol{\eta}) - \sum_{n=1}^{\infty} \left(\frac{2}{n\pi} \right) \exp\left(-n^2\pi^2\tau\right) \sin n\pi\eta \tag{5.22}$$

This solution consists of a steady state limit and a transient term that vanishes as time increases. This solution is, of course, an approximation and it fails to correctly predict the velocity at very small times and large values of b as the fluid near the stationary plate cannot feel the presence of the moving plate.

5.3 Appendix C

In this section, we include an explanation about the orthogonal quality and aspect ratio calculations as criteria for mesh quality.

- Orthogonal quality: Orthogonal quality is an important indicator of mesh quality, and it is defined by calculating the following dot products: The normalized dot product of two vectors A_i and f_i. Ai is the area vector of a face while f_i is the vector from the centroid of the cell to the centroid of that face. The following graphic shows the vectors used in calculating orthogonal quality:

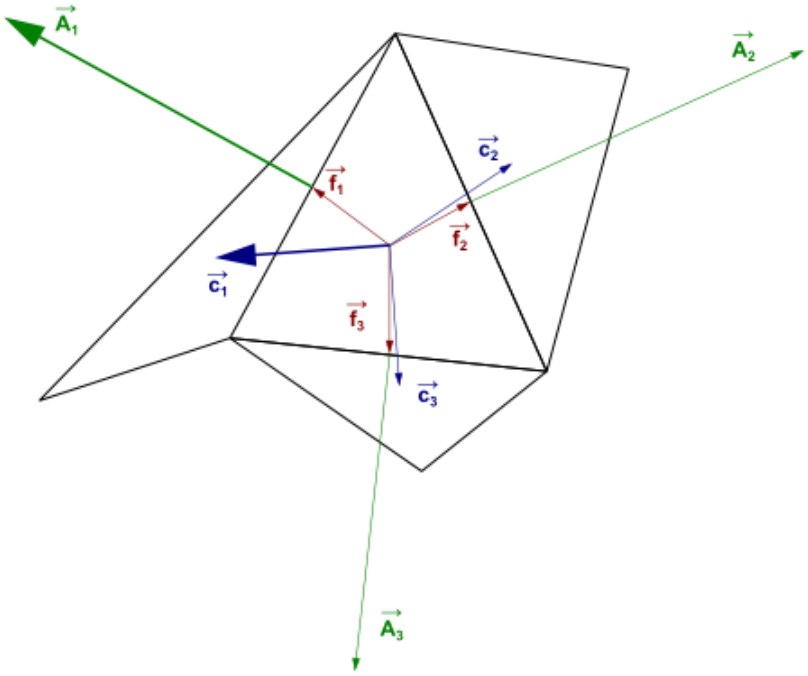

Figure 5.3: Vectors used in calculating orthogonal quality

The dot product of Ai and fi is calculated using the following equation:

$$\frac{(A_i * f_i)}{(|A_i||f_i|)} \tag{5.23}$$

The second normalized dot product is that of the area vector of a face (A_i) dotted to a vector from the centroid of the cell to the centroid of the adjacent cell that shares that face (c_i). These vectors are seen in the figure above. This dot product is calculated using equation 2.2 with changing fi with ci:

$$\frac{(A_i * c_i)}{(|A_i||c_i|)} \tag{5.24}$$

After calculating both dot products, the minimum value of both dot products for all of the faces is then defined as the orthogonal quality of a cell. The worst cells have an orthogonal quality close to 0, while the best cells have an orthogonal quality closer to 1.

- Aspect Ratio: Aspect ratio is a measure of the stretching of a cell. It is defined as the ratio of maximum value to minimum value of the normal distance between the cell centroid and the face centroids. The following graphic shows the lengths A and B that are used in calculating the aspect ratio:

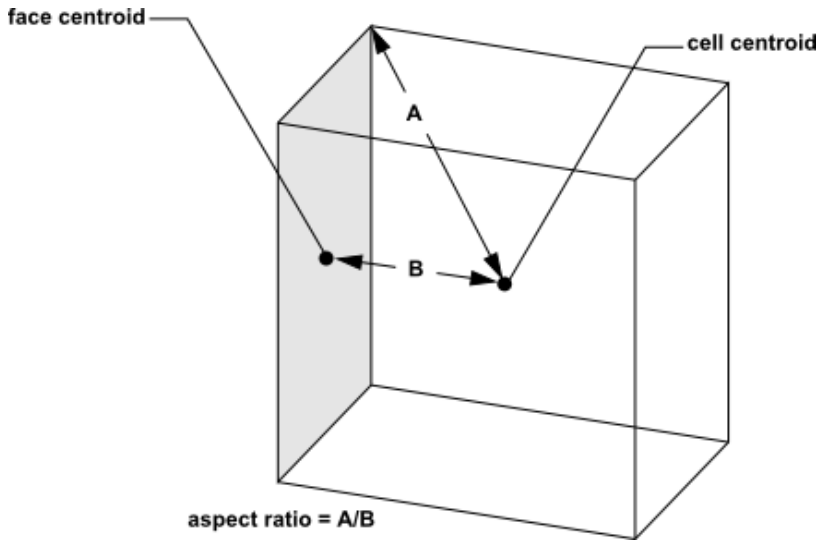

Figure 5.4: Aspect Ratio calculation schematic